

THE ROLE OF STARBURST-AGN COMPOSITES IN LUMINOUS INFRARED GALAXY MERGERS: INSIGHTS FROM THE NEW OPTICAL CLASSIFICATION SCHEME

T.-T. YUAN, L. J. KEWLEY AND D. B. SANDERS

Institute for Astronomy, University of Hawaii, 2680 Woodlawn Drive, Honolulu, HI 96822

Accepted by ApJ

ABSTRACT

We investigate the fraction of starbursts, starburst-AGN composites, Seyferts, and LINERs as a function of infrared luminosity (L_{IR}) and merger progress for ~ 500 infrared-selected galaxies. Using the new optical classifications afforded by the extremely large data set of the Sloan Digital Sky Survey, we find that the fraction of LINERs in IR-selected samples is rare ($< 5\%$) compared with other spectral types. The lack of strong infrared emission in LINERs is consistent with recent optical studies suggesting that LINERs contain AGN with lower accretion rates than in Seyfert galaxies. Most previously classified infrared-luminous LINERs are classified as starburst-AGN composite galaxies in the new scheme. Starburst-AGN composites appear to “bridge” the spectral evolution from starburst to AGN in ULIRGs. The relative strength of the AGN versus starburst activity shows a significant increase at high infrared luminosity. In ULIRGs ($L_{\text{IR}} > 10^{12} L_{\odot}$), starburst-AGN composite galaxies dominate at early – intermediate stages of the merger, and AGN galaxies dominate during the final merger stages. Our results are consistent with models for IR-luminous galaxies where mergers of gas-rich spirals fuel both starburst and AGN, and where the AGN becomes increasingly dominant during the final merger stages of the most luminous infrared objects.

Subject headings: galaxies: evolution — galaxies: interactions — galaxies: starburst — galaxies: active — infrared: galaxies

1. INTRODUCTION

Luminous Infrared Galaxies (LIRGs: $L_{\text{IR}} > 10^{11} L_{\odot}$) were first discovered in small numbers ~ 4 decades ago (Low & Kleinmann 1968; Kleinmann & Low 1970a,b; Becklin et al. 1971; Becklin & Neugebauer 1972; Rieke & Low 1972a). The importance of these objects to galaxy evolution was made more clear following the first all-sky survey carried out by the *Infrared Astronomical Satellite* (IRAS; Neugebauer et al. 1984). Soifer et al. (1987) found that the space density of infrared (IR)-selected LIRGs in the local Universe ($z < 0.1$) rivaled that of the most powerful optically-selected starburst and Seyfert galaxies at similar bolometric luminosity, and that the most luminous objects – ultraluminous infrared galaxies (ULIRGs: $L_{\text{IR}} > 10^{12} L_{\odot}$) – had similar space densities and bolometric luminosities as optically-selected quasi-stellar objects (QSOs).

There have been numerous studies related to the origin and evolution of U/LIRGs², and most now seem to agree that strong interactions and mergers of gas-rich galaxies are the trigger for the majority of the more luminous LIRGs (see the review by Sanders & Mirabel 1996). The merger fraction increases with IR luminosity and approaches 100% for samples of ULIRGs (e.g., Sanders et al. 1988a; Kim 1995a; Clements et al. 1996; Farrah et al. 2001). In the complete sample of IRAS 1 Jy ULIRGs by Kim (1995a), 117 out of 118 galaxies show strong signs of tidal interaction (Veilleux et al. 2002).

There is less consensus on the nature of the power source

of U/LIRGs. It is clear that the IR luminosity in U/LIRGs can derive from dust reprocessing of either extreme starburst activity, Active Galactic Nuclei (AGN), or a combination of the two. Studies of moderate to large samples of U/LIRGs (e.g., Kim 1995a; Veilleux et al. 1995; Goldader et al. 1995; Genzel et al. 1998) indicate that the dominant power source in lower luminosity LIRGs is an extended starburst, and that an AGN often makes an increasing contribution to the bolometric luminosity in the more luminous sources with obvious energetic point-like nuclei. However, different studies of the same objects disagree on the relative contributions of starburst and AGN activity to the bolometric luminosity, in particular for the ULIRGs where the dominant energy source powering their extremely luminous and compact nuclear cores continues to be the subject of intense debate (c.f., Joseph 1999; Sanders 1999). Although numerous studies at various wavelengths continue to be carried out to determine the energy source of ULIRGs (e.g., Tran et al. 2001; Farrah et al. 2003, 2007; Lípári et al. 2003; Ptak et al. 2003; Imanishi et al. 2007), determining the relative contribution of starbursts and AGN within individual galaxies is still difficult.

One of the commonly proposed merger scenarios for ULIRGs (e.g., Sanders et al. 1988a; Kim et al. 1995b; Farrah et al. 2001; Lípári et al. 2003; Dasyra et al. 2006) is based on the Toomre & Toomre (1972) sequence in which two galaxies lose their mutual orbital energy and angular momentum to tidal features and/or an extended dark halo and coalesce into a single galaxy. Tidal interactions and associated shocks are thought to trigger star formation (e.g., Bushouse 1987; Kennicutt et al. 1987; Liu & Kennicutt 1995; Barnes 2004) which heats the surrounding dust, producing strong far-infrared (FIR) radiation. The FIR radiation rises to an ultra-luminous IR stage powered by starbursts and/or dust-shrouded AGN. As starburst activity subsides, the merger finally evolves into an optically bright QSO. In this scenario, ULIRGs plausibly represent a dust-

Electronic address: yuan@ifa.hawaii.edu, kewley@ifa.hawaii.edu, sanders@ifa.hawaii.edu

¹ $L_{\text{IR}} \equiv L(8 - 1000 \mu\text{m})$; (see Sanders & Mirabel 1996)

² Previous studies of the properties of infrared galaxies versus $\log(L_{\text{IR}}/L_{\odot})$ often divide the galaxy samples into decade luminosity bins and use the terms moderate, luminous, ultraluminous, and hyperluminous to refer to the decade ranges 10–10.99, 11–11.99, 12–12.99, and 13–13.99, respectively. We follow this convention here, and use U/LIRGs when we wish to refer to all galaxies with $\log(L_{\text{IR}}/L_{\odot}) = 11 - 12.99$.

shrouded transition stage that leads to the formation of optical QSOs (*e.g.*, Sanders et al. 1988b; Dasyra et al. 2006; Kawakatu et al. 2006; Zauderer et al. 2007).

A key element in testing the above scenario is to clarify the power source behind the strong IR emission, and the relationship between this power source and the evolutionary stage of the interaction. Comprehensive studies on large IR-selected samples are crucial to this analysis. Notable examples of such samples are the IRAS Bright Galaxy Survey (BGS: Veilleux et al. 1995), the IRAS 1 Jy ULIRGs sample (1 Jy ULIRGs: Kim 1995a; Kim & Sanders 1998; Veilleux et al. 2002), and the Southern Warm Infrared Galaxy sample (SW01: Kewley et al. 2001a).

Most previous studies use standard optical spectral diagnostic diagrams to classify the dominant power source in emission-line galaxies (Baldwin, Phillips, & Terlevich 1981; Veilleux & Osterbrock 1987). These diagrams are based on four optical emission line ratios that are sensitive to the hardness of the ionizing radiation field. More recently, the Sloan Digital Sky Survey (SDSS) has revolutionized these classification schemes by revealing clearly formed branches of star-forming galaxies, Seyferts, and Low Ionization Narrow Emission-line Region Galaxies (LINERs) on the diagnostic diagrams, for the first time (Kewley et al. 2006). Kewley et al. shows that many galaxies previously classified as LINERs lie along a well-defined mixing branch from star-forming galaxies to Seyfert galaxies.

In light of this new classification scheme, we investigate the new spectral classification of IR galaxies as a function of IR luminosity and merger progress. We describe our sample selection and derived quantities in § 2. The results are presented in § 3. We discuss the results in § 4 and summarize in § 5. For convenience of comparison with the old 1 Jy ULIRG analysis by Veilleux et al. (1999, 2002), we adopt a Hubble constant of $H_0 = 75 \text{ km s}^{-1} \text{ Mpc}^{-1}$, and $\Omega_m = 0.27$, $\Omega_\Lambda = 0.73$ throughout the paper.

2. SAMPLE SELECTION AND DERIVED QUANTITIES

2.1. Sample Selection

We use three local samples of IR-selected galaxies: the 118 ULIRGs from the IRAS 1 Jy sample of ULIRGs (Kim & Sanders 1998) (hereafter the 1 Jy ULIRGs sample), 104 of the highest luminosity objects from the IRAS Bright Galaxy Survey (hereafter the BGS sample), and the complete sample of 285 galaxies in the Southern Warm Infrared Galaxies sample (Kewley et al. 2001a) (hereafter the SW01 sample).

The complete 1 Jy sample was compiled by Kim (1995a) and is described in detail in Kim & Sanders (1998). The 1 Jy sample was selected from the IRAS Faint Source Catalog (FSC) with flux $F(60\mu\text{m}) > 1 \text{ Jy}$ at high Galactic latitude $|b| > 30^\circ$, and declination $\delta > -40^\circ$. The sample contains 118 objects with redshift $z = 0.02 - 0.27$ and $\log(L_{\text{IR}}/L_\odot) = 12.00 - 12.90$. Veilleux et al. (1999) published optical spectra for 108 of these objects at a resolution of 8.3 Å. Their nuclear spectra were extracted using a window corresponding to a physical diameter of 4 kpc (for the three objects with $z > 0.2$: IRAS 00397–1312, IRAS 12032+1707, and IRAS 23499+2434, a diameter of 8 kpc was used). Typical uncertainties for the emission line ratios are 5%–10%. A *R*- and *K'*-band image atlas for the 1 Jy sample is given in Kim et al. (2002) and the analysis of the morphological properties was carried out by Veilleux et al. (2002).

We also include 104 lower luminosity objects from the IRAS BGS (Sanders et al. 1995; Veilleux et al. 1995; Soifer et al. 1986, 1987, 1989). The BGS represent all extragalactic sources brighter than 5.24 Jy at $60\mu\text{m}$, $|b| > 5^\circ$. Kim et al. (1995b) provide optical spectra for 114 of these objects at a resolution of 8–10 Å. A constant linear aperture of 2 kpc was used to extract the nuclear spectra. The redshift range is $z = 0.0027 - 0.09$ with a median of 0.02. Among the original 114 BGS objects in Kim et al. (1995b), a total of 10/114 are ULIRGs, with 8 of the ULIRGs also included in the 1 Jy sample. We only use the 104 LIRGs ($\log(L_{\text{IR}}/L_\odot) < 12.0$) in the BGS sample. *The main role of the BGS sample in this study is to supplement the 1 Jy ULIRG sample with lower luminosity objects, and to help create a larger non-ULIRGs sample in § 3.4.* The final L_{IR} range is $\log(L_{\text{IR}}/L_\odot) = 10.5 - 13.0$ for the 1 Jy ULIRG and BGS samples combined.

The SW01 sample was selected by Kewley et al. (2001a) from the catalog of Strauss et al. (1992). It consists of 285 IRAS galaxies with $F(60\mu\text{m}) > 2.5 \text{ Jy}$ at $|b| > 15^\circ$, $\delta < 0^\circ$. Kewley et al. (2001a) applied the “warm” color criteria ($F_{60}/F_{25} < 8$) to ensure that the sample contains a high fraction of AGN. SW01 has a wide coverage in IR luminosity, and is dominated by LIRGs: among the total 285 galaxies, 277 galaxies have $\log(L_{\text{IR}}/L_\odot) = 8.0 - 11.99$ and 8 are ULIRGs. Kewley et al. (2001a) took high-resolution spectra (30 km s⁻¹ at H α) for 235 objects in the SW01 sample (the emission line intensity measurements are accurate to within 30%). The SW01 redshift limit is $z < 0.027$ for IR luminosities $\log(L_{\text{IR}}/L_\odot) < 11.0$ and $z < 0.067$ for $\log(L_{\text{IR}}/L_\odot) > 11.0$. Their nuclear spectra were extracted using an aperture corresponding to 1 kpc at the redshift of each galaxy.

For the BGS and SW01 samples, we use optical images from the Digitized Sky Survey (DSS) and *K_s*-band images from 2MASS. We use the *K_s*-band images to obtain the projected nuclear separation for the interacting galaxies in our samples and we use the *R*-band and other available optical band images for identification of tidal debris.

2.2. Optical Classification

The classification of the dominant energy source in emission line galaxies using optical emission-line ratios was first proposed by Baldwin, Phillips, & Terlevich (1981, hereafter BPT). BPT proposed the use of the [O III] $\lambda 5007/\text{H}\beta$, [N II] $\lambda 6583/\text{H}\alpha$, and [O I] $\lambda 6300/\text{H}\alpha$ line ratios for spectral classification, taking advantage of the sensitivity of these line ratios to the hardness of the ionizing radiation field. Kennicutt & Keel (1984) and Keel (1983) extended the initial set of classification ratios to include the [S II] $\lambda\lambda 6716, 6731/\text{H}\alpha$ line ratio which is also sensitive to the hardness of the ionizing radiation field and observable in the optical regime. To improve the optical classification, Osterbrock & de Robertis (1985) and Veilleux & Osterbrock (1987, hereafter VO87) derived the first semi-empirical classification lines to be used with the standard optical diagnostic diagrams. Because of the pioneering work of Baldwin, Phillips, & Terlevich (1981) and Veilleux & Osterbrock (1987), the “standard optical diagnostic diagrams” based on the [O III]/H β , [N II]/H α , [S II]/H α , and [O I]/H α line ratios are commonly known as BPT or VO87 diagrams.

Large samples or active galaxies reveal a tight abundance sequence for star-forming galaxies and an AGN sequence that

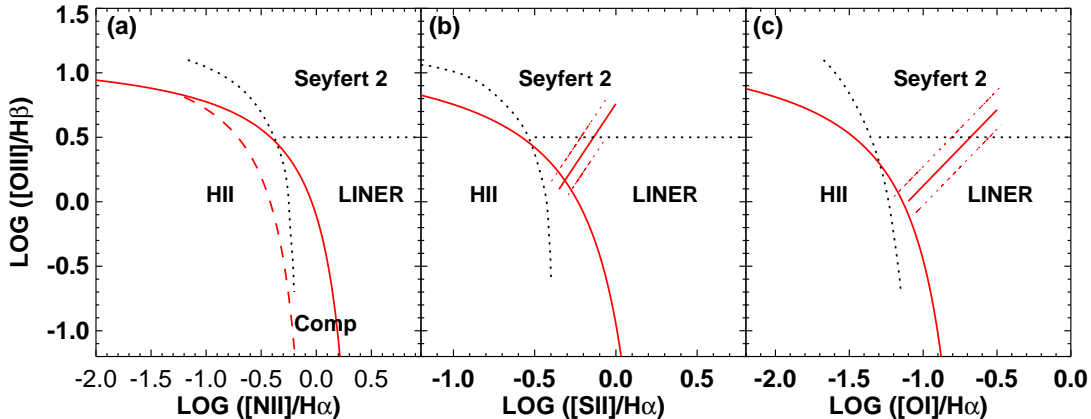


FIG. 1.— Standard optical diagnostic diagrams showing the previous optical classification scheme by Veilleux & Osterbrock (1987) (black dotted lines) and the new classification scheme by Kewley et al. (2006). Star-forming galaxies form a tight abundance sequence on these diagnostic diagrams. The AGN branch begins at the metal-rich end of the star-forming galaxy sequence and extends towards the upper right corner of these diagrams. Red solid curves are the theoretical “maximum starburst line” derived by Kewley et al. (2001b) as an upper limit for star-forming galaxies (see more descriptions in section 2.2); the red dashed curve on the [N II] diagram is the Kauffmann et al. (2003) semi-empirical lower boundary for the star-forming galaxies; the red lines (with the empirical error ± 0.1 dex lines) on [S II] and [O I] diagrams are the empirical boundary lines between Seyfert 2 galaxies and LINERS. See § 2.2 for more details. The Kewley et al. (Ke06) scheme substantially changes the LINER boundaries, and includes a class for starburst-AGN composites (labeled Comp). Note that in the [N II] $\lambda 6583/\text{H}\alpha$ versus [O III]/H β diagram (panel a), the VO87 scheme distinguishes between Seyfert 2 galaxies and LINERS, while the Ke06 classification scheme does not.

begins at the metal-rich end of the star-forming abundance sequence and extends towards the upper-right corner of the diagnostic diagrams (i.e. towards large [O III]/H β , [N II]/H α , [S II]/H α , and [O I]/H α).

The first purely theoretical classification scheme was developed by Kewley et al. (2001b) (hereafter Ke01). Ke01 used a combination of modern stellar population synthesis, photoionization, and shock models to derive a “maximum starburst line” on the BPT diagrams. Galaxies that lie above this line can not be explained by any combination of starburst models and require a dominant ($> 50\%$) contribution from an AGN. Galaxies that lie below the Ke01 line may include a non-dominant (i.e. $< 50\%$) contribution from an AGN.

To obtain a more stringent sample of star-forming galaxies, Kauffmann et al. (2003) (hereafter Kau03) shifted the Ke01 line to form a semi-empirical upper boundary for the star-forming branch observed with the SDSS. The Kau03 line retains the shape of the Ke01 theoretical models, with a shift to enable classification of pure star-forming galaxies (i.e. 100% star-formation dominated). The combination of the Ke01 and Kau03 lines serves to separate pure star-forming galaxies, galaxies that are likely to contain both star-formation and AGN activity (composite galaxies), and galaxies that are dominated by their AGN.

Kewley et al. (2006, hereafter Ke06) showed that AGN sequence forms two clear branches on the [S II]/H α and [O I]/H α diagnostic diagrams. These two branches were revealed with the large number of SDSS galaxies ($\sim 45,000$); these branches were not observed with the smaller sample sizes (~ 200) that were used in previous studies (e.g., VO87 and Ke01). Ke06 derived empirical boundary lines between Seyfert 2s and LINERS on the [S II]/H α and [O I]/H α diagrams based on the observed local minimum between the Seyfert and LINER branches. Seyfert and LINER galaxies defined in this way have significant differences in their host properties; LINERS are older, more massive, less dusty, and less concentrated than Seyfert galaxies. However at fixed accretion rate, these differences disappear. LINERS and Seyferts form a continuous sequence in Eddington rate from low to high Eddington rates, respectively. Ke06 conclude that LIN-

ERS are AGN and that the dichotomy between Seyferts and LINERS is analogous to the high and low states observed in X-ray binary systems.

As in X-ray binaries, LINERS have a harder ionizing radiation field and lower ionization parameter than Seyfert galaxies. These characteristics make the [S II]/H α and [O I]/H α diagrams ideal for separating Seyferts and LINERS. The [S II] and [O I] emission-lines are produced in the partially ionized zone at the edge of the nebula; this zone is large and extended for hard radiation fields. Power-law AGN models from Groves, Dopita & Sutherland (2004) indicate that models with a hard radiation field and low ionization parameter are separated in the [S II]/H α and [O I]/H α diagrams; these ratios change by ~ 0.7 dex as the power-law index is changed from -1.2 to -2.0.

Note that the [N II]/H α ratio diagram can not be used to separate Seyferts and LINERS. The [N II]/H α ratio is only weakly dependent on the hardness of the radiation field; $\log([\text{N II}]/\text{H}\alpha)$ only changes by 0.2 dex as the power-law index is varied from -1.2 to -2.0 (Groves, Dopita & Sutherland 2004). The [N II]/H α ratio is much more strongly dependent on the metallicity of the nebular gas. Metallicity differences among AGN host galaxies plus the weak dependence on hardness renders the [N II]/H α diagram insensitive to the major differences between Seyfert and LINERS seen in the [S II]/H α and [O I]/H α diagrams.

Ke06 estimated empirical errors (± 0.1 dex) for the Seyfert-LINER boundary by considering the positions of galaxies that remain Seyfert 2 or that remain LINER in both the [S II]/H α and [O I]/H α diagrams. The class of galaxies that lie within ± 0.1 dex of the Seyfert 2/LINER line is uncertain.

In Fig. 1 we show the difference between the previous VO87 classification scheme (black dotted lines) and the new Ke06 classification scheme (red solid and dashed lines). Galaxies that were previously classified as LINERS may be either (a) true LINERS, (b) composite HII-AGN galaxies, or (c) Seyfert 2 galaxies, or (d) high metallicity star-forming galaxies, according to the new classification scheme. A substantial fraction ($\sim 1/3$) of ULIRGs and LIRGs have been previously classified as LINERS using the VO87 method (Veilleux et al.

1995, 1999). Therefore, the application of the Ke06 classification scheme may reveal new insight into the power source behind IR-selected galaxies previously classified as LINERs.

In addition to the major change in LINER classification, the Ke06 scheme includes starburst-AGN composite galaxies as a separate class of objects. The $[\text{N II}]/\text{H}\alpha$ versus $[\text{O III}]/\text{H}\beta$ diagram is used to classify composite galaxies. (Composite galaxies lie between the red dashed and solid lines in Fig. 1a.) The $[\text{N II}]/\text{H}\alpha$ ratio is more sensitive to the presence of a low-level AGN than the $[\text{S II}]/\text{H}\alpha$, and $[\text{O I}]/\text{H}\alpha$ line ratios because the $[\text{N II}]/\text{H}\alpha$ ratio is a linear function of nebular metallicity until high metallicities where the $[\text{N II}]/\text{H}\alpha$ reaches a plateau at $\log([\text{N II}]/\text{H}\alpha) \sim -0.5$ (Kewley & Dopita 2002; Denicoló, Terlevich & Terlevich 2002; Pettini & Pagel 2004). At this plateau, any AGN contribution shifts the $[\text{N II}]/\text{H}\alpha$ ratio above $\log([\text{N II}]/\text{H}\alpha) > -0.5$. An AGN contribution to low metallicity galaxies is extremely rare (Groves, Heckman & Kauffmann 2006).

We apply the new Ke06 classification scheme to our three samples to discriminate between star-forming galaxies (or starburst/HII-region galaxies), Seyfert 2, LINERs, and starburst-AGN composites. In Fig. 2, our three samples are shown in comparison with the SDSS galaxies used in Kewley et al. (2006) on the BPT diagrams with the new classification boundaries. The Ke06 classification scheme that we use in this work is as follows:

(1) Star-forming galaxies: lie below and to the left of Kau03 line on the $[\text{N II}]/\text{H}\alpha$ diagram (e.g., Fig. 2 left column, the lower red solid line), and below and to the left of Ke01 theoretical lines in the $[\text{S II}]/\text{H}\alpha$ and $[\text{O I}]/\text{H}\alpha$ diagrams (e.g., Fig. 2 middle and right columns, the red solid lines).

(2) Starburst-AGN composites: lie above Kau03 line but below and to the left of Ke01 theoretical line in the $[\text{N II}]/\text{H}\alpha$ diagram (Fig. 2 left column).

(3) Seyfert 2 galaxies: lie above the Ke01 theoretical lines on all three BPT diagrams and also above the Seyfert-LINER boundary lines in the $[\text{S II}]/\text{H}\alpha$ and $[\text{O I}]/\text{H}\alpha$ diagrams (e.g., Fig. 2 middle and right columns).

(4) LINERs: lie above the Ke01 theoretical lines on all three BPT diagrams and below the Seyfert-LINERs boundary lines on the $[\text{S II}]/\text{H}\alpha$ and $[\text{O I}]/\text{H}\alpha$ diagrams.

(5) Ambiguous galaxies: are those that are classified as one type of object in one or two diagrams and are classified as another type in the remaining diagram(s).

(6) Seyfert 1 galaxies: *are not included on the BPT diagrams and are considered separately*. They are characterized by their broad Balmer emission lines – usually $\text{H}\alpha(FWHM) > 5 \times 10^3 \text{ km s}^{-1}$. Thus, galaxies classified as Seyfert 1 in previous studies remain classed as Seyfert 1 in our study.

The most stringent method for classification of galaxies using this scheme is to use all three diagnostic diagrams. We refer to the use of all three diagnostic diagrams hereafter as the “3-of-3” criterion. The use of all three diagnostic diagrams allows for ambiguous galaxies to be classified separately. For data sets with a significant fraction of unmeasurable or uncertain $[\text{S II}]/\text{H}\alpha$ or $[\text{O I}]/\text{H}\alpha$ ratios, an alternative “2-of-3” criterion is often applied. This method applies the majority class, i.e. if 2 out of 3 diagnostic diagrams give one class, but the third diagram gives a different class or is unavailable, the consistent class of the 2 remaining diagnostic diagrams is assumed. There is no ambiguous class if the 2-of-3 criterion is applied. Most previous studies on the optical classification of IR galaxies apply the 2-of-3 criterion (Veilleux et al. 1995,

1999, 2002). The $[\text{S II}]/\text{H}\alpha$ classifications are uncertain for a substantial portion ($\sim 16 - 17\%$) of the BGS and 1 Jy ULIRG samples (i.e. the $[\text{S II}]/\text{H}\alpha$ class lies within the 0.1 dex uncertainty line defined in Ke01). For comparison with previous work and to avoid contamination by uncertain $[\text{S II}]/\text{H}\alpha$ classifications, we apply the “2-of-3” criterion to our samples. We discuss our results in the context of the 3-of-3 criterion in the Appendix B.

In the 1 Jy ULIRG sample, the 2-of-3 classification scheme yields 8 (7.8%) star-forming galaxies, 46 (44.7%) starburst-AGN composites, 35 (33.9%) Seyfert 2, 10 (9.7%) Seyfert 1, and 4 (3.9%) LINERs. These classes include the 9 galaxies in the 1 Jy sample with double nuclei that have spectra taken for both nuclei. Of these double nuclei galaxies, 4 galaxies have consistent classes for both nuclei and are assigned composite (3/4) and Seyfert 2 (1/4) classes respectively. The remaining 5 double nuclei galaxies have a composite nucleus plus either a starburst nucleus (4/5) or a Seyfert 2 nucleus (1/5). Because their overall class is uncertain, we exclude these 5 double nuclei galaxies from our sample. We note that our results are unchanged if we randomly assign these double nuclei galaxies the class of either nucleus.

The BGS sample covers lower IR luminosities than the 1 Jy ULIRG sample and has a larger portion of star-forming galaxies. The 2-of-3 classification scheme gives 30 (25.97%) star-forming galaxies, 32 (41.56%) starburst-AGN composites, 19 (24.67%) Seyfert 2, 1 (1.3%) Seyfert 1, and 5 (6.5%) LINERs. These classifications include 13 galaxies with double nuclei in which both nuclei have consistent classes (7/13 star-forming and 6/13 composites). We do not include an additional 5 double nuclei galaxies with differing classes for each nucleus. Our results are not affected if we randomly assign these double nuclei galaxies the class of either nucleus.

There are 175 galaxies in the SW01 sample that have measured emission line ratios with $S/N > 3\sigma$. The SW01 sample covers substantially IR lower luminosities than the BGS or 1 Jy ULIRG samples and contains a large fraction of star-forming galaxies. In the 2-of-3 scheme, the SW01 sample contains 78 (41.7%) star-forming galaxies, 57 (30.5%) starburst-AGN composites, 40 (21.4%) Seyfert 2, 10 (5.3%) Seyfert 1, and 2 (1.1%) LINERs. These statistics include 12 double nuclei galaxies with consistent classifications for both nuclei (7/12 star-forming galaxies, 3/12 composites, and 2/12 Seyfert 2 galaxies). We do not include 4 double nuclei galaxies that have different spectral types for each nucleus. Our results remain unchanged if we randomly assign these 4 galaxies the class of either nucleus.

Our classifications for the 1 Jy ULIRG, BGS, and SW01 samples are listed in Tables 1, 1 and 1, respectively. For comparison, in Table 1 and 1, we also list the classifications given in Veilleux et al. (1999) using the traditional VO87 method.

2.3. AGN Contribution

Ke06 showed that the SDSS galaxies form a mixing sequence between pure star-forming galaxies and pure AGN. They defined an empirical linear distance (D_{SF}) from the star-forming sequence for both the Seyfert and LINER branches on the $[\text{O III}]/\text{H}\beta$ vs $[\text{O I}]/\text{H}\alpha$ diagnostic diagram. The $[\text{O III}]/\text{H}\beta$ vs $[\text{O I}]/\text{H}\alpha$ diagram was used to derive this distance because in this diagram, the Seyfert and LINER branches are clearly separated (unlike the $[\text{O III}]/\text{H}\beta$ vs $[\text{N II}]/\text{H}\alpha$ diagram where the Seyfert and LINER branches coincide). Fig. 2 shows that unlike the optically-selected SDSS galaxies, the majority of IR-selected galaxies do not lie

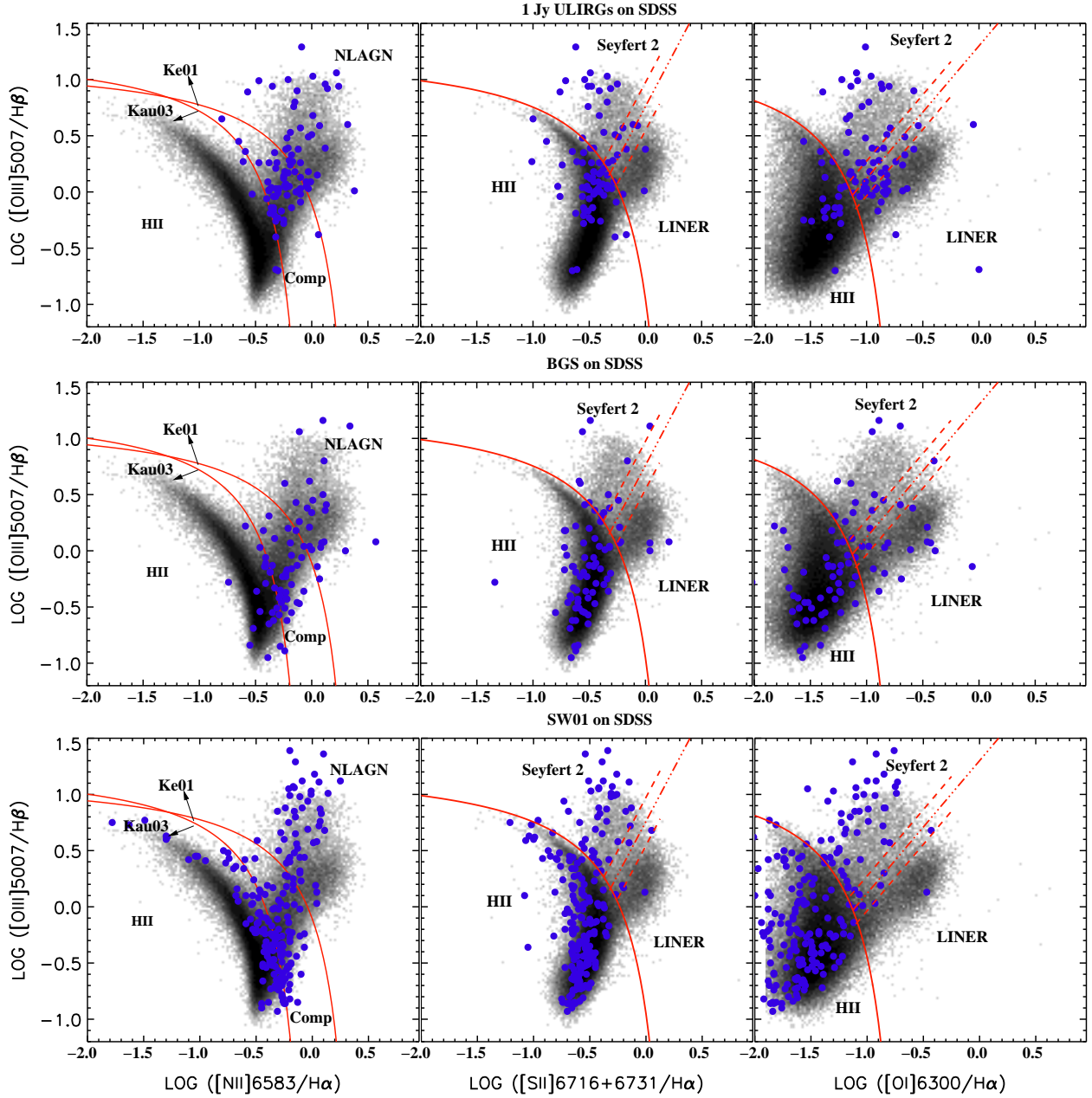


FIG. 2.— Samples (blue filled circle) used in this work are shown on the BPT diagrams, over-plotted are the SDSS galaxies (black dots) from Kewley et al. (2006). The curves and lines have the same meaning as in Fig. 1, i.e., upper red curves on all three BPT diagrams are the theoretical “maximum starburst line”; the lower red curve on the [N II] diagram is the Kauffmann et al. (2003) semi-empirical lower boundary for star-forming galaxies, and the red lines (with the empirical error ± 0.1 dex lines) in [S II] and [O I] diagrams are the empirical boundary lines between Seyferts and LINERs. See the text in § 2.2 for more details. From top to bottom, the samples are: 1 Jy ULIRGs, BGS, and SW01. The red lines are the new classification scheme Kewley et al. (2006) used to separate starburst (HII-region) galaxies, starburst-AGN composite galaxies, Seyfert 2, and LINERs. In the leftmost panels, NLAGN \equiv narrow emission-line AGN (Seyfert 2 plus LINERs); Comp \equiv starburst-AGN composites.

along the pure star-forming galaxy sequence; most IR galaxies lie in the composite and AGN regions of the diagnostic diagrams. Because of this difference, it is more intuitive to think of the linear distance between the star-forming sequence and the AGN region on the [O III]/H β vs [O I]/H α diagnostic diagram as the relative contribution of an (D_{AGN}) for IR-selected galaxies.

The quantity D_{AGN} can be defined other standard diagnostic diagrams with negligible difference. In Appendix A, we

investigate alternative definitions of D_{AGN} , and the relationship between D_{AGN} and spectral class. Because D_{AGN} is a relative measure, our results remain the same regardless of how D_{AGN} is defined. Note that because D_{AGN} is defined as a distance (in dex) in log line-ratio space, it does not give the fraction or a percentage of star-formation or AGN emission in a galaxy. D_{AGN} gives a *relative* indication of the relative contribution of AGN to the EUV radiation field from galaxy to galaxy. The absolute value of D_{AGN} is abstract, and D_{AGN}

should be used only in relation to other galaxies. For example, a galaxy with $D_{\text{AGN}} = 0.6$ does not correspond to an AGN contribution of 60%. D_{AGN} is useful only for relative comparisons, for example, a galaxy with $D_{\text{AGN}} = 0.6$ is likely to have a larger contribution from an AGN than a galaxy with a smaller D_{AGN} .

In Fig. 3, we show D_{AGN} on the [O III]/H β vs [O I]/H α diagram, relative to the Ke06 classification scheme (red lines). By definition, $D_{\text{AGN}} = D_{\text{SF}}$ from Ke06. Pure star-forming galaxies have $D_{\text{AGN}} = 0$. The mixing sequence from pure star-forming galaxies to the tip of the AGN branch begins at $D_{\text{AGN}} \geq 0$, and lies below the maximum starburst line (red curve in Fig. 3). Galaxies that are classed as composites in the [O III]/H β vs [N II]/H α diagram have $D_{\text{AGN}} \leq 0.5$ or 0.6 (green curve). Galaxies that have $D_{\text{AGN}} = 1$ are likely to have line ratios that are strongly dominated by an AGN, although some contribution from star formation can not be ruled out.

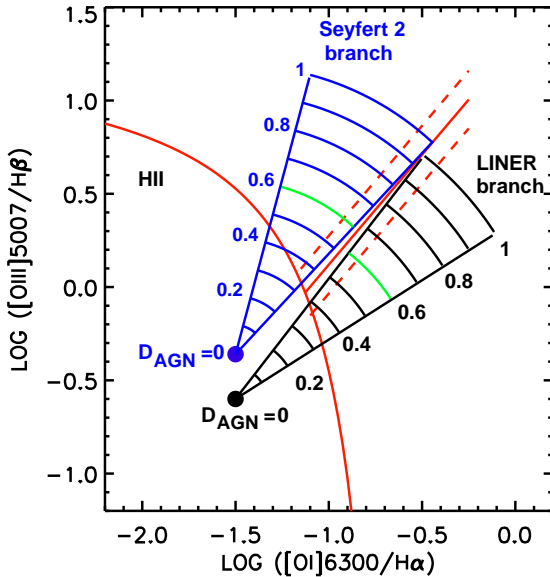


FIG. 3.— [O I]/H α versus [O III]/H β diagnostic diagram showing the Ke06 classification scheme (red lines), and the distance to the peak of the AGN branch, D_{AGN} . Blue and black curves give lines of constant D_{AGN} , respectively. The green curves indicate the maximum D_{AGN} for starburst-AGN composite galaxies (defined in the [N II]/H α versus [O III]/H β diagram). Starburst galaxies and some starburst-AGN composite galaxies lie below the Ke06 maximum starburst line (red curve) in this diagram.

2.4. Merger Progress Tracers

We use two tracers of merger progress: merger morphology, and projected nuclear separation (ns). We adopt the morphological classification scheme outlined in Veilleux et al. (2002). Veilleux et al. (2002) relate galaxy morphology to merger stage using numerical simulations of galaxy mergers (Barnes & Hernquist 1992, 1996):

1. Wide binary: “binary systems” with projected separation $ns > 10$ kpc.
2. Close binary: “binary systems” with projected separation $ns < 10$ kpc.
3. Diffuse merger: single systems ($ns \sim 0$) with tidal features, and with $L_{K4\text{kpc}}/L_K < 1/3$, where $L_{K4\text{kpc}}$ means the

K -band luminosity within 4 kpc and L_K is the total luminosity.

4. Compact merger: single systems ($ns \sim 0$) with tidal features, and with $L_{K4\text{kpc}}/L_K > 1/3$.

5. Old merger: single systems ($ns \sim 0$) with no unmistakable signs of tidal tails, yet have disturbed central morphologies.

We use the the projected separation measured in the K_s -band and the length of the tidal tails measured in R -band by Veilleux et al. (2002) for the 1 Jy sample.

For the BGS and SW01 samples, we use 2MASS K_s -band images and the IRAF “imcntr” task to measure the projected nuclear separations. We use R -band DSS images to determine the morphological classification according to the Veilleux et al. scheme. We search for companions within a 100 kpc radius. The maximum angular radius available for 2MASS images is 10 arcminutes, giving galaxies at redshifts $z < 0.0087$ images less than 100 kpc wide. For these low redshift galaxies, we use DSS images that have larger angular radii so that the 100 kpc search radius criterion is always satisfied. “Isolated systems” defined in this way are therefore confined within the 100 kpc region. It is possible that these systems are interacting with objects wider than 100 kpc. For the few galaxies without available 2MASS images, we used the data from other images in NED or from the literature. These objects are noted in Tables 1, 1, and 1.

For BGS LIRGs, we find that 42/77 are mergers, and 35/77 are isolated systems or have companions outside the 100 kpc search radius. For the remaining 37 BGS objects, the image quality is too poor for morphological classification. We do not include these 37 galaxies in the morphological study. Therefore the morphological classification for the BGS sample is incomplete. We emphasize here that the main role of the BGS sample in this study is to supplement the 1 Jy ULIRG sample with lower luminosity objects, and to help create a larger non-ULIRGs sample in § 3.4.

The SW01 sample is not dominated by late stage mergers (class 3, 4, 5 above) and only 33/285 can be definitively identified as mergers with $ns \sim 0$. A significant fraction (156/285) of SW01 galaxies show no obvious signs of merging or interaction. For statistical significance, we combine the “diffuse”, “compact”, and “old” merger stages as one “single merger” stage so that each class contains at least 10 galaxies.

The final morphological classes for the SW01 and BGS samples are:

1. Wide binary: “binary systems” with projected separation $ns > 10$ kpc.
2. Close binary: “binary systems” with projected separation $ns < 10$ kpc.
3. Single merger: single systems ($ns \sim 0$) with tidal features or distorted nuclei recognizable in available images.
4. Isolated system: systems that have no obvious signs of merging or interaction, within the 100 kpc image search radius.

There may be some overlap in the “isolated” and “single-merger” groups, as it is impossible to distinguish whether a galaxy is truly “isolated” or is simply at the end of the merging stage where all the tidal features disappear (or are too faint to be observed). For example, there are 7 single nucleus ULIRGs in the SW01 sample that do not show obvious signs of merging in available NED images. However, 1 Jy R -band images show remnant signs of tidal activity for 3 of the single nuclei galaxies.

Besides the uncertainty in distinguishing the “isolated sys-

tems” from “single mergers”, there are some classical drawbacks in using projected separation as a tracer for merger processes:

a) Projection effects may randomize the results. However, for a large sample, projection effects should be statistically unimportant; on average, interacting systems with $ns \lesssim$ few kpc are likely to be at a later stage in the merger process than systems with $ns \gtrsim$ a few 10 kpc.

b) Merger models such as Barnes & Hernquist (1992, 1996) show that ns is not necessarily a linear function of time: the projected separation decreases in a period of close contact (“first-pass”) and then increases again before the nuclei finally merge.

c) Projected nuclear separation can not trace merger progress in multiple mergers of more than two galaxies unless the time between current mergers and that of the former mergers is sufficiently large to enable any merger-induced star formation and AGN activity to subside (Borne et al. 2000). This issue may be a potential problem for the SW01 sample, in which some galaxies are in the Hickson Compact Groups (Garcia 1993). In these groups, the IR emission may be triggered by the weak interaction between the group members. For the 1 Jy sample, multiple mergers are not a major concern because deep images indicate that only 5/118 ($< 5\%$) are *possible* multiple mergers (Veilleux et al. 2002).

With these caveats in mind, we calculate the projected separation between paired galaxies in our samples using 2MASS K_s -band images for the BGS and SW01 samples, and the Veilleux et al. (2002) K_s -band projected separation measurements for the 1 Jy sample.

3. RESULTS

3.1. Spectral Type as a Function of IR luminosity

Our samples span different luminosity ranges and have different IR color selection criteria. To examine how spectral type changes with IR luminosity, we combine the 1 Jy ULIRG sample with the BGS sample to cover a broad IR luminosity range and to facilitate comparisons with the classical Veilleux et al. (1999) result. We consider the SW01 sample separately in this case because the warm color criterion of the SW01 sample may affect how the spectral type changes with IR luminosity.

Fig. 4 shows the optical spectral type as a function of L_{IR} for the combined 1 Jy and BGS samples. The results are also tabulated in Table 1. It is obvious from this figure that LINERs are rare compared with other spectral classes in our IR-luminous samples, with only 3% LINERs in the 1 Jy sample and 7% in the BGS sample. The 1 Jy ULIRGs sample may lack LINERs because this sample is selected at larger redshifts than the SDSS. Ke06 showed that the fraction of LINERs in the SDSS falls at $z > 0.1$ due to incompleteness. The lack of LINERs in SW01 may be at least partly caused by the warm selection criterion, as the “warm” criterion selects against LINERs (Kewley et al. 2001a).

We find few IR-luminous LINERs found in our samples. A majority (72/79) of the objects previously classified as LINERs are classified as composite galaxies and Seyfert 2s using the Ke06 SDSS-based classification scheme. LINERs in the SDSS-based classification scheme contain an older stellar population and an AGN with a lower accretion rate than Seyfert 2 galaxies. The lack of such LINERs in IR samples indicates that (a) bona fide IR-luminous LINERs are quite rare — only 3/108 in the 1 Jy ULIRG sample and 5/97 in the BGS

samples, and (b) in most cases, LINERs do not contain the intense star formation and/or the strong dust-reprocessed AGN emission responsible for the IR luminosities seen in U/LIRGs. We discuss the rare IR-selected LINERs in more detail in § 4.1.

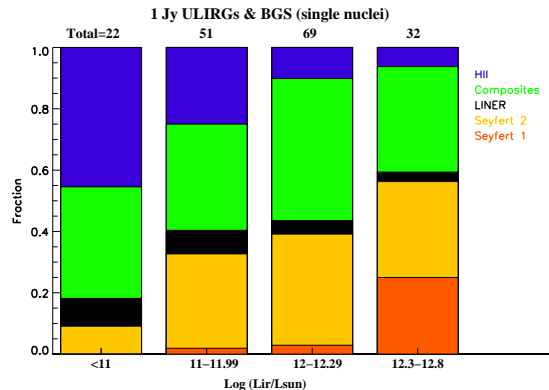


FIG. 4.— Spectral type (2-of-3 criterion) as a function of L_{IR} for the 1 Jy ULIRG sample (Veilleux et al. 1999) and the LIRGs in the BGS sample (Veilleux et al. 1995). Similar to Veilleux et al. (1999), double nucleus objects are excluded in this figure. The number of galaxies contained in each bin is marked on top of the histogram. The luminosity bins are labeled at the bottom. Throughout this paper we will always use grey for ambiguous, blue for HII-region galaxies, green for composites, black for LINERs, yellow for Seyfert 2 galaxies and orange for Seyfert 1 galaxies, unless otherwise specified. The result of applying the stringent 3-of-3 criterion is presented in Appendix B.

Interestingly, we find that Seyfert 1 galaxies favor higher L_{IR} , consistent with previous studies suggesting that Seyfert 2 galaxies have weaker mid-IR luminosities than Seyfert 1 galaxies (Heckman 1995; Maiolino et al. 1995; Giuricin, Mardirossian & Mezetti 1995) (however, see Bonatto, & Pastoriza 1997; Haas et al. 2007). However, because the 1 Jy ULIRG + BGS samples only contain a total of 11 Seyfert 1 galaxies, a larger number of IR-luminous Seyfert 1s is required to determine the significance of this result.

The spectral type as a function of L_{IR} for the SW01 sample is shown in Fig. 5 and Table 1. Because the SW01 sample covers a lower IR luminosity range, the SW01 sample is intended to extend the 1 Jy ULIRG and BGS samples to lower luminosities, rather than to serve as a comparison sample. Nevertheless, in panel (a) of Fig. 5, the L_{IR} bins are chosen to be the same as the first two bins of Fig. 4 to facilitate comparisons between the warm (SW01) and non-warm (BGS and 1 Jy ULIRG) samples over the L_{IR} range where all samples are well-defined.

Since our samples contain a large number of objects with $L_{\text{IR}}/L_{\odot} < 10^{10}$, L_{IR} is divided into sub-bins in panel (b) to improve resolution. Bin sizes are chosen to ensure that each bin contains at least 20 galaxies. In the SW01 sample, the AGN fraction increases and the fraction of starbursts decreases as L_{IR} becomes larger, similar to the trend in the 1 Jy ULIRG + BGS samples. As shown in panel (b) of Fig. 5, the lowest luminosity bin ($L_{\text{IR}}/L_{\odot} < 10^{10}$) has the largest fraction of star-forming galaxies.

3.2. D_{AGN} as a function of L_{IR}

Spectral types only reflect the galaxy’s general position on the BPT diagrams. To investigate the relative contribution from an AGN as a function of IR luminosity, we show in Fig. 6

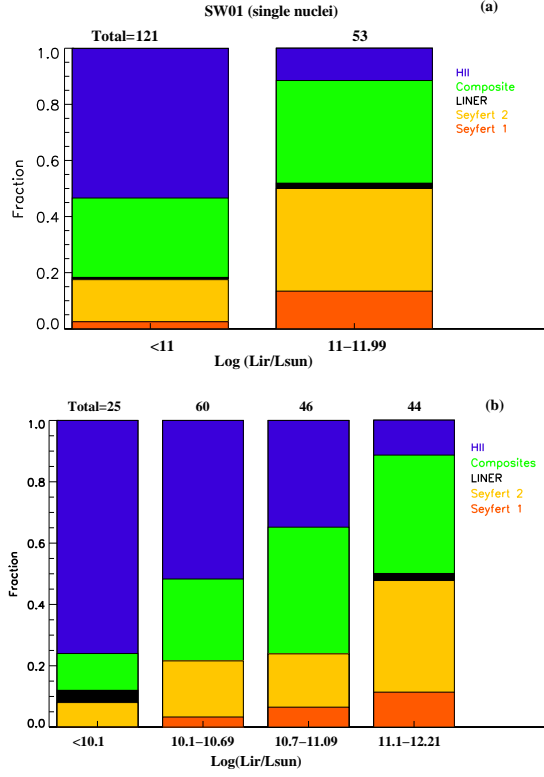


FIG. 5.— Optical classification results as a function of L_{IR} for the SW01 sample. The SW01 sample is dominated by moderate IR luminosity $L_{\text{IR}} < 10^{11} L_{\odot}$ sources, with $\sim 25\%$ LIRGs, and very few ULIRGs ($< 2\%$ = 3 objects). For comparison with Figure 4, Panel (a) divides the SW01 sample into the same two lower luminosity bins (only 3 SW01 objects have $L_{\text{IR}} > 10^{12} L_{\odot}$ in the bin $12 < \log(L_{\text{IR}}/L_{\odot}) < 12.21$). Panel (b) provides a finer grouping into four L_{IR} bins to gain more resolution. The sub-bins are chosen in such a way that each bin contains at least 20 galaxies.

and Fig. 7 D_{AGN} as a function of L_{IR} for the combined 1 Jy ULIRG + BGS sample, and the SW01 sample, respectively. The mean, median, and standard errors for D_{AGN} are calculated for the same four luminosity ranges as used in Fig. 4 and Fig. 5b, for the combined 1 Jy ULIRG + BGS sample and the SW01 sample, respectively. To test whether the distribution of D_{AGN} in each L_{IR} bin can be drawn randomly from the same parent population, we perform the two-sample Kolmogorov-Smirnov (KS) test to each pair of neighboring L_{IR} bins. For the L_{IR} bin pairs (1-2), (2-3), (3-4) in Fig. 6, the KS test gives a probability $P_{\text{null}} = 0.08, 3.98\text{E-}6, \text{ and } 0.16$ that the distributions are drawn from the same parent population, indicating a statistically significant change in the D_{AGN} distribution at the 90% confidence level between $10^{10} < L_{\text{IR}}/L_{\odot} < 10^{12.3}$ for the 1 Jy ULIRG + BGS sample.

For the SW01 L_{IR} bin pairs (1-2), (2-3), (3-4) in Fig. 7, the KS test gives a probability $P_{\text{null}} = 0.48, 0.28, \text{ and } 0.02$ that the distributions are drawn from the same parent population, indicating a statistically significant change in the D_{AGN} distribution at the 98% confidence level between $10^{10.7} < L_{\text{IR}}/L_{\odot} < 10^{12.3}$. The rise in D_{AGN} at lower luminosities is not statistically significant for the SW01 sample.

We conclude that the rise of D_{AGN} with L_{IR} is significant for all three samples at $L_{\text{IR}}/L_{\odot} > 10^{11.0}$. Previous studies indicate that the fraction of AGN increases at large L_{IR} (e.g., Armus, Heckman, & Miley 1990; Veilleux et al. 1995; Goto 2005). Figures 6 and 7 confirm these results.

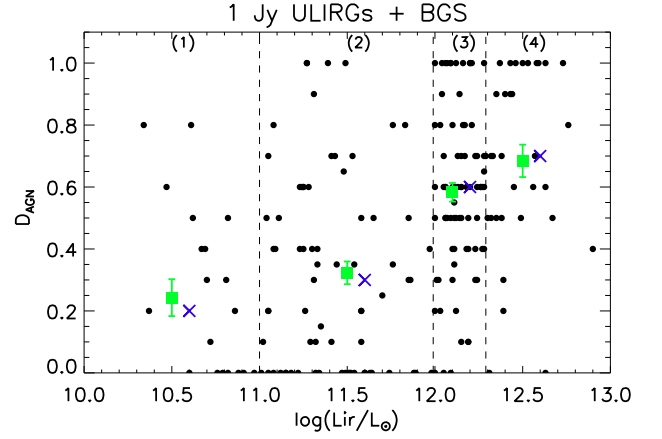


FIG. 6.— D_{AGN} as a function of L_{IR} for the 1 Jy ULIRG + BGS sample. The mean, median, and standard error of the mean for the same 4 IR luminosity bins used in Fig. 4 are plotted in green. Blue crosses give the median values. The probability that the D_{AGN} distribution in consecutive bin pairs is drawn from the same parent population is given in § 3.2. The rise in D_{AGN} from luminosity bin (2) to (3) and bin (3) to (4) is significant at the 99% and 90% confidence levels, respectively

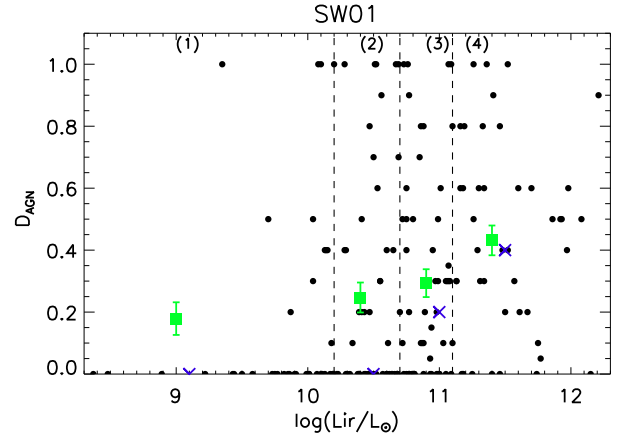


FIG. 7.— D_{AGN} as a function of L_{IR} for the SW01 sample. The mean, median, and standard error of the mean for the same 4 IR luminosity bins used in Fig. 5 panel (b) are plotted in green. Blue crosses give the median values. The probability that the D_{AGN} distribution in consecutive bin pairs is drawn from the same parent population is given in § 3.2. The rise in D_{AGN} from luminosity bin (3) to (4) is significant at the 98% confidence level

3.3. Spectral type as a function of morphology/merger stage

Following the morphological definitions in § 2.4, in Fig. 8 we give the spectral type as a function of merging stage for the 1 Jy ULIRG sample. The dashed line indicates the uncertainty in classification associated with the double nuclei galaxies that have differing classifications for each nucleus. These galaxies are discussed in more detail in Appendix C.

The key significant features in Figure 8 are:

1) The fraction of starburst-AGN composite galaxies reaches a peak at the diffuse merger stage, indicating that both merger-induced starburst activity, and AGN fueling contribute to the total energy budget at the diffuse merger stage.

2) The fraction of starburst-AGN composite galaxies falls sharply at the later merger stages (compact and old merger), giving rise to a larger portion of Seyfert galaxies rises in these later merger stages. We suggest that starburst-AGN composite galaxies evolve into Seyferts as merger-induced starburst activity subsides.

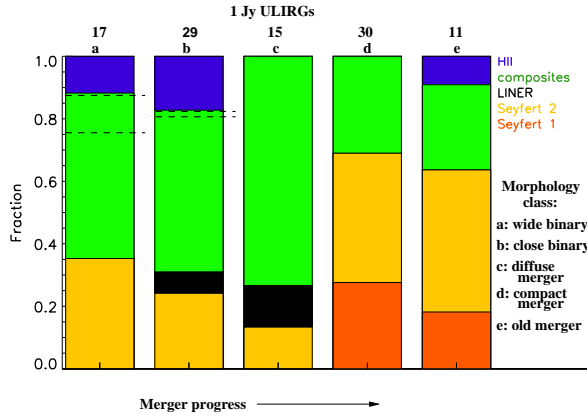


FIG. 8.— Optical spectroscopic classification as a function of merger morphology for the 1 Jy ULIRG sample. The merger progresses from left to right: a. wide binary, b. close binary, c. diffuse merger, d. compact merger, e. old merger. No “isolated” class is defined for the 1 Jy morphology class since there is only one isolated object in this sample. The number of galaxies in each morphology class is marked on top of each bin, and is given in Table 1. The fraction of composite galaxies reaches a peak at the diffuse merger stage. The fraction of AGN-dominated (Seyfert 2 and Seyfert 1) rises at later merger stages (compact and old merger). Dashed lines give the range of uncertainty in the fraction of HII and composites associated with the double nuclei galaxies with different spectral types for each nucleus (see Appendix C).

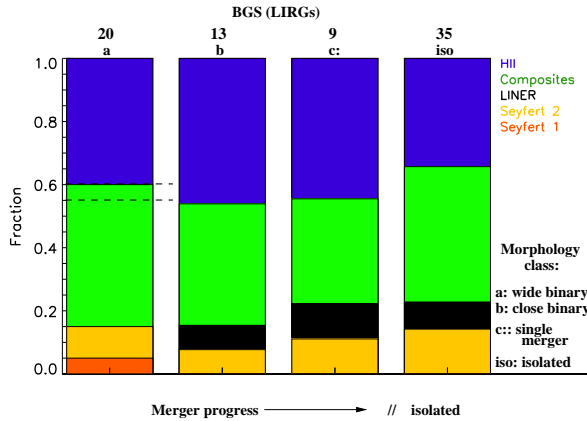


FIG. 9.— Spectral type as a function of morphology for the LIRGs in the BGS sample. The merger progresses from left to right: a. wide binary, b. close binary, c.: single-merger, iso. isolated system. Dashed lines give the range of uncertainty in the fraction of HII and composites caused by the double nuclei galaxies with different spectral types for each nucleus. The single-merger stage combines the diffuse, compact, and old merger stages to ensure sufficient numbers of objects for statistically meaningful comparisons between the morphological types. There may be overlap between single merger and isolated stages due to surface brightness effects.

Figure 8 also shows potentially interesting trends that are limited by small numbers for the 1 Jy ULIRG sample:

- (1) The fraction of Seyfert galaxies appears to decrease ($41 \pm 16\%$ c.f. $13 \pm 9\%$) between the wide binary stage (stage a) to the diffuse merger stage (stage c).
- (2) Seyfert 1 galaxies only occur at the later merger stages (d and e in Figure 8)

A larger sample of ULIRGs is required to verify these two trends.

We show the spectral type as a function of merger morphology for the BGS and SW01 samples in Figures 9 and 10 respectively. The results are listed in Table 1 and Table 1. Clearly, for objects with L_{IR} lower than that of ULIRGs, there is no strong change in spectral classification as a func-

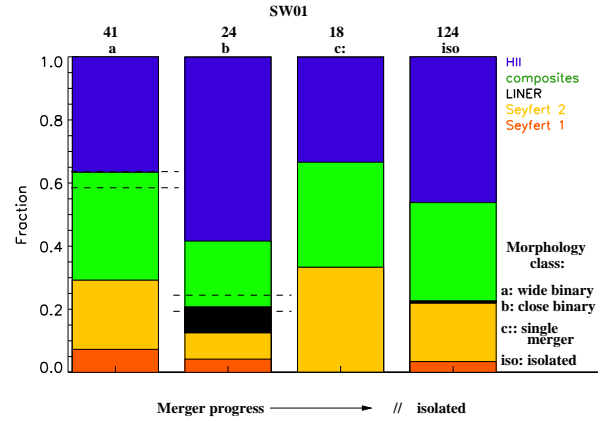


FIG. 10.— Optical spectroscopic classification as a function of merger morphology for the SW01 sample. The merger progresses from left to right: a. wide binary, b. close binary, c.: single merger, d. isolated. Dashed lines give the range of uncertainty in the fraction of HII and composites (in stage a), composite and Seyferts (in stage b) caused by the double nuclei galaxies with different spectral types for each nucleus. The single-merger stage combines the diffuse, compact, and old merger stages to ensure sufficient numbers of objects for statistically meaningful comparisons between the morphological types. The SW01 sample contains a substantial fraction ($156/285 \sim 54\%$) of apparently isolated galaxies. There may be overlap between single merger and isolated stages due to surface brightness effects. The fraction of composites is not significant as compared to Fig. 8.

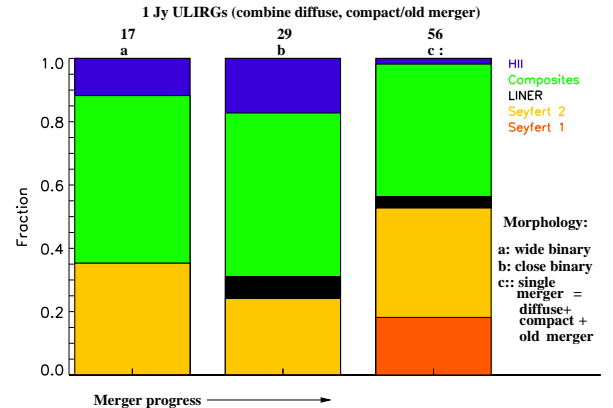


FIG. 11.— Optical spectroscopic classification as a function of merger morphology for the 1 Jy ULIRG sample, after combining the diffuse, compact and old mergers as one single merger category.

tion of merger progress. However, the BGS and SW01 samples do not contain a sufficient number of galaxies in the single merger stage that have deep enough images to allow separation into diffuse, compact, and old merger stages where the largest changes in spectral class occur for ULIRGs. The fraction of merging galaxies in the SW01 and BGS samples is 45% and 54%, respectively, compared with 99% for the 1 Jy ULIRG sample. In addition, most of the merging systems in the SW01 and BGS samples are in the earlier, binary stages rather than the advanced single-merger stages in the 1 Jy ULIRG sample (11% in the SW01 sample, and 12% in the BGS sample versus 50% in the 1 Jy ULIRG sample). If we combine objects in the 1 Jy ULIRG sample which have diffuse, compact, and old merger types into one single merger class (Fig. 11), the changes seen in Fig. 10 disappear. These results highlight the need for sensitive K - and B -band imaging to distinguish between the three late merger stages (diffuse, compact, and old merger) in non-ULIRG samples.

To conclude, the 1 Jy ULIRG sample shows a marked change in galaxy spectral type as a function of merger progress, especially, composite galaxies dominate the diffuse merger stage. It is unclear whether such a change occurs in the lower luminosity BGS and SW01 samples. We note that the relative lack of galaxies at late merger stages in the lower luminosity samples may indicate that a ULIRG phase occurs before or at the single nucleus stage, in at least some IR-selected galaxies.

3.4. D_{AGN} and L_{IR} versus ns

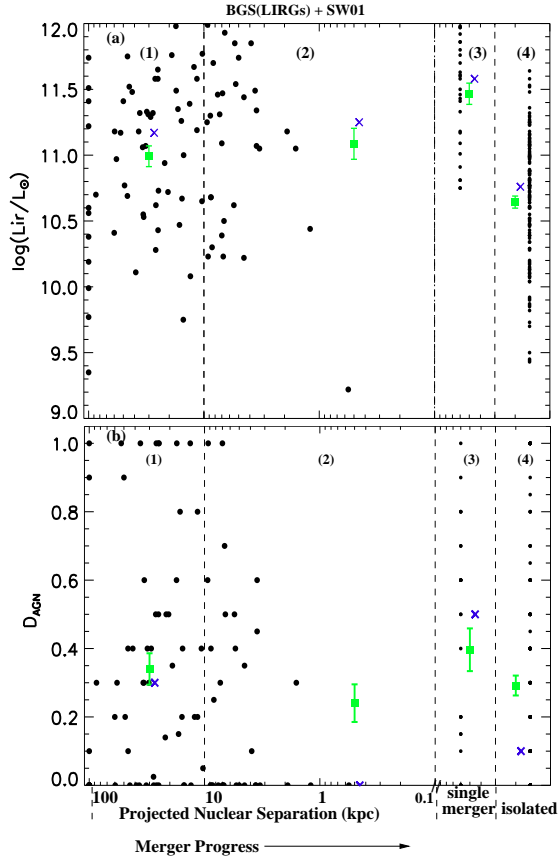


FIG. 12.— (a) L_{IR} as a function of projected nuclear separation for the BGS (LIRGs only) and SW01 samples combined. (b) Distance from the starburst sequence D_{AGN} as a function of projected nuclear separation for the combined BGS (LIRGs only) and SW01 samples. The mean and 1σ standard deviation of the mean for D_{AGN} are plotted as green squares. Median values are shown as blue crosses. The vertical regions from left to right are: (1) binary systems with nuclear separation $ns > 10$ kpc. (2) binary systems with nuclear separation $ns < 10$ kpc. (3) single-merger systems. (4) isolated systems. The BGS and SW01 samples are combined in order to get a larger non-ULIRG sample. For the 21 overlap objects in the two samples, mean values of D_{AGN} are taken. KS tests for the significance of the difference in y-axis distributions are given in § 3.4.

To investigate the merger progress in a morphology-independent way, we compare the *relative* contribution of an AGN (D_{AGN}) and L_{IR} as a function of projected nuclear separation (ns). We first investigate the non-ULIRG samples by combining the BGS and SW01 samples to (a) reach statistically significant conclusions (thus minimizing projection effects) and (b) span a broad range of L_{IR} . The ns values for both samples are measured using 2MASS or DSS images, and the two samples exhibit similar behavior in spectral type versus morphology as discussed in § 3.3.

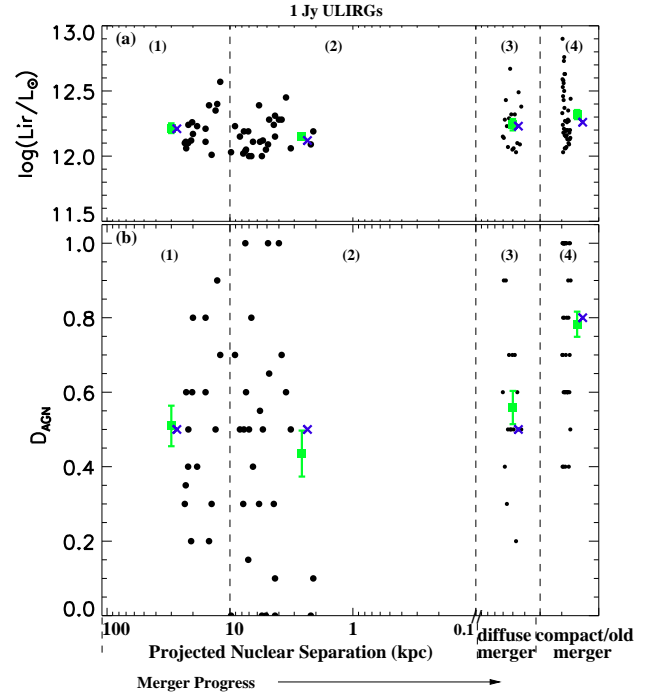


FIG. 13.— (a) L_{IR} as a function of projected nuclear separation for the 1 Jy ULIRGs. (b) Distance from the starburst sequence D_{AGN} as a function of projected nuclear separation for the 1 Jy ULIRG sample. The means and 1σ standard deviation of the mean for D_{AGN} are plotted as green squares. Median values are shown as blue crosses. The vertical regions from left to right are: (1) binary systems with nuclear separation $ns > 10$ kpc. (2) binary systems with nuclear separation $ns < 10$ kpc. (3) single-mergers with diffuse nuclei. (4) single-mergers with compact/old nuclei. KS tests for the significance of the difference in y-axis distributions are given in § 3.4.

In Figure 12(a), we show the infrared luminosity, L_{IR} , of the merger pair as a function of nuclear separation. Fig. 12(b) gives D_{AGN} as a function of nuclear separation for the BGS (LIRGs) and the SW01 samples combined. These figures indicate that D_{AGN} is constant at ~ 0.3 within the errors at all merger stages in these 2 samples. The mean value of L_{IR} is constant within the errors through the wide and close pair stages, and then rises by a factor of ~ 2 in the single merger stage. We performed KS tests to determine the significance of the distribution of D_{AGN} and L_{IR} as a function of projected separation. For the distribution of data within adjacent L_{IR} bins (1) and (2), (2) and (3), and (3) and (4) in Fig. 12a, the KS test indicates a probability $P_{\text{null}} = 0.89, 0.04,$ and $3.8\text{E}-9$ respectively that the adjacent data sets are drawn from the same parent population. For the adjacent D_{AGN} bins (1) and (2), (2) and (3), (3) and (4) in Fig. 12b, the KS test indicates a probability $P_{\text{null}} = 0.13, 0.18,$ and 0.16 that the adjacent data sets are drawn from the same parent population. We conclude that both the rise in L_{IR} from close pair to single merger stage and the fall in L_{IR} from single merger to isolated stages are significant at the 95% and 99.99% level respectively. There are no statistically significant changes in D_{AGN} as a function of projected separation for the non-ULIRG BGS and SW01 samples.

In Figure 13(a) and Figure. 13(b) we show the L_{IR} and D_{AGN} versus projected separation for the 1 Jy ULIRG sample. Like the lower luminosity pairs, D_{AGN} is constant within the errors as a function of projected separation until the diffuse merger stage. The mean D_{AGN} is larger than seen in the lower luminosity BGS+SW01 sample (~ 0.52 c.f. 0.3). The

most obvious difference in the behavior of ULIRGs with projected separation compared with the lower luminosity pairs, occurs in the final compact/old merger phase where ULIRGs show a rather dramatic increase in D_{AGN} to a mean value of ~ 0.8 . This rise is statistically significant at the 95% level; the KS test indicates a probability $P_{\text{null}} = 0.46, 0.51,$ and 0.05 that adjacent data sets (1-2), (2-3), (3-4) are drawn from the same parent population. This rise in D_{AGN} is consistent with the rise in the Seyfert fraction with merger progress seen in § 3.3, particularly in the emergence of Seyfert 1s at the compact and old merger stages. The rise in D_{AGN} is not accompanied by a significant rise in the mean L_{IR} (the KS test indicates a probability $P_{\text{null}} = 0.52, 0.12,$ and 0.84 that the adjacent data sets (1-2), (2-3), (3-4) are drawn from the same parent population).

Our results confirm previous observational (e.g., Sanders et al. 1988a) and theoretical (e.g., Mihos & Hernquist 1994) studies showing that the maximum L_{IR} is produced close to the time when the two nuclei merge.

4. DISCUSSION

4.1. IR-selected LINERS

We find that IR luminous LINERS are rare compared to other optical spectral types, even in the low-redshift BGS sample. A majority of the previously classified IR-luminous LINERS are now reclassified as starburst-AGN composites in the new SDSS optical spectroscopic classification scheme. This result prompts us to discuss the following issues: (1) The relationship between the new class of LINERS and starburst-AGN composite objects. (2) The nature of IR-luminous LINERS compared with the LINERS from the SDSS. We discuss each of these issues separately below.

(1) Kewley et al. (2006) have shown that the host properties of composite galaxies are intermediate between those of AGN and high metallicity star-forming galaxies, and that LINERS form a unique, coherent class that is distinct from Seyferts, star-forming galaxies and composites. Specifically, LINERS are older, more massive, less dusty and less concentrated than Seyfert galaxies. These optical results highlight the intrinsically different nature of LINERS and composites.

Here we investigate whether similar differences exist in popular mid-IR diagnostics. In Figure 14, we investigate the positions of galaxies on the $[\text{FeIII}] 26.0\mu\text{m}/[\text{OIV}] 25.9\mu\text{m}$ versus $[\text{OIV}] 25.9\mu\text{m}/[\text{NeIII}] 12.8\mu\text{m}$ diagnostic diagram. This diagram separates star-forming galaxies from those dominated by an AGN. Previously, IR-luminous LINERS occupied a region in between starburst and Seyfert galaxies, whereas IR-faint LINERS occupied a region offset from the starburst-Seyfert sequence (Sturm et al. 2006). In our new classification scheme, only 1 out of the 16 IR-luminous LINERS are classified as LINERS (the rest 15 objects are 8 composites, 1 Seyfert 2s, and 6 ambiguous classes between HII and Seyfert 2s), while 10 out of the 17 IR-faint LINERS remain LINERS (the rest 7 objects are ambiguous classes between LINERS and Seyfert 2s). Figure 14 indicates that the majority (9/13) of the composites lie in along a mixing sequence connecting star-forming galaxies and Seyferts. By contrast, most (8/10) of the LINERS lie offset from the mixing sequence. These results are consistent with our view of optically selected LINERS as a different class of objects from starburst-AGN composites.

(2) There is growing evidence that a large fraction of optically selected LINERS are low luminosity AGN with low

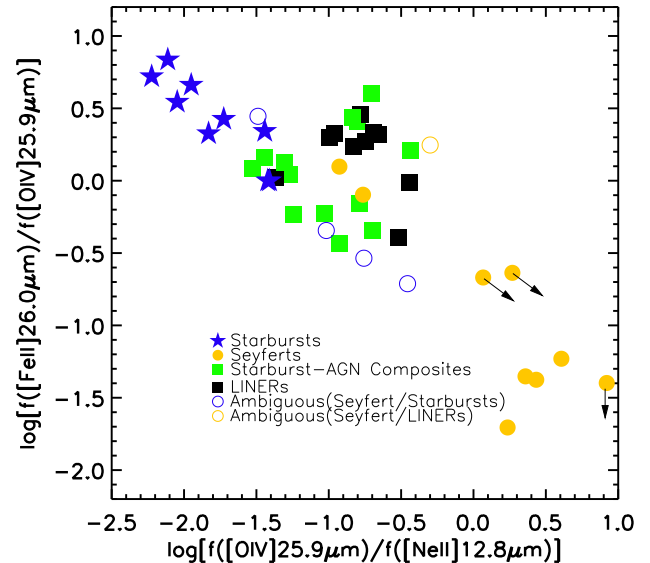


FIG. 14.— Mid-infrared diagnostic from Sturm et al. (2006), with objects re-classified using the Ke06 new scheme. The data were provided by Sturm, E. The symbol meanings are labeled on the plot. The bracket after the ambiguous class indicates between which classes the ambiguity lies.

accretion rates (e.g., Ho 1999; Quataert et al. 2001; Barth 2002). The SDSS LINER population studied by Kewley et al. (2006) supports this AGN nature. They show that at fixed $L[\text{O III}]/\sigma^4$ (an indicator for the black hole accretion rate), all differences between Seyfert and LINER host properties disappear. With this interpretation of LINERS, it is not surprising that we find so few IR-luminous LINERS because ULIRGs tend to harbor AGN that favor high-accretion rates (Weedman 1983; Filippenko & Sargent 1985; Sanders et al. 1988a). Theory supports this interpretation; numerical simulations predict that the black hole accretion rate rises rapidly during the merger process when enormous quantities of gas flows into the central regions of the merging galaxies (e.g., Taniguchi et al. 1999; Hopkins et al. 2005).

What about the few IR-luminous LINERS that do exist in our samples? Do they belong to the same class as optical LINERS? In Table 1 we list all the possible LINERS found in our combined 1 Jy ULIRG + BGS + SW01 sample. Altogether there are 9 objects in the three samples that fall into our LINER class, however, only 4/9 of these LINERS (Arp 220 in the 1 Jy ULIRG sample, NGC 6240 in the SW01/BGS samples and another 3 in the BGS sample) can be “safely” classified as LINERS. The other 5/9 LINERS lie near the 0.1 dex error region of the Seyfert-LINER boundaries, and may be Seyfert objects or intermediate between Seyfert and LINER types. This can be clearly seen in Figure 15, where all 9 LINERS are over-plotted with the SDSS data from Kewley et al. (2006) on the $[\text{S II}]/\text{H}\alpha$ versus $[\text{O III}]/\text{H}\beta$ and $[\text{O I}]/\text{H}\alpha$ versus $[\text{O III}]/\text{H}\beta$ diagnostic diagrams.

In Figure 15, we indicate the positions of two well-studied IR-luminous LINERS: NGC 6240 and Arp 220. Recent high resolution X-ray and radio data for NGC 6240 (Lira et al. 2002; Komossa et al. 2003; Iono et al. 2007) and Arp 220 (Clements et al. 2002; Ptak et al. 2003; Downes & Eckart 2007) provide convincing evidence for the existence of AGN in these 2 objects. However, the LINER emission may be excited by other ionization processes. Both of these two LIN-

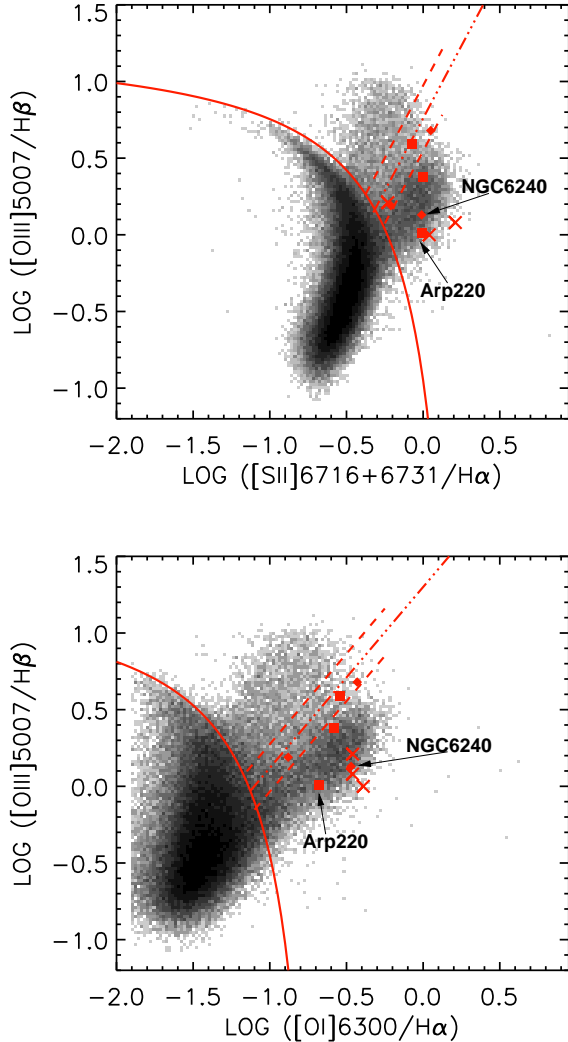


FIG. 15.— The positions of the 9 LINERs on the $[SII]/H\alpha$ versus $[OIII]/H\beta$ and $[OI]/H\alpha$ versus $[OIII]/H\beta$ diagrams over-plotted on the SDSS data from Kewley et al. (2006). The 3 IR-luminous LINERs in the 1 Jy ULIRG sample are shown as squares, the 3 IR-luminous LINERs in the SW01 sample are shown as diamonds, and the 3 crosses are the IR-luminous LINERs from the BGS sample.

ERs show evidence for starburst-driven superwinds and/or shocks that may dominate the EUV emission of these galaxies (Heckman et al. 1987b; Tecza et al. 2000; Lira et al. 2002; McDowell et al. 2003; Iwasawa et al. 2005). Further investigation into the EUV power source of IR-luminous LINERs is required to draw robust conclusions about the nature of the few IR-luminous LINERs in our samples.

To summarize, the rarity of IR-luminous LINERs is consistent with the picture that most LINERs are (a) excited by low Eddington rate black holes and (b) reside in galaxies with an aged stellar population. The special cases of Arp 220 and NGC 6240 may indicate a contribution from different LINER ionization sources: either starburst superwinds or shocks driven by galaxy collisions.

4.2. Are starburst-AGN composites playing the role of “bridging” in LIRGs and ULIRGs?

In Fig. 16, we show 5 different galaxy samples on the $[NII]/H\alpha$ versus $[OIII]/H\beta$ diagnostic diagram. The new Ke06 classification boundaries are indicated in red. We supplement the 1 Jy ULIRG, BGS and SW01 samples with two optically selected samples: the NFGS field galaxy sample (Jansen et al. 2000) and the BGK00 galaxy close pair sample (Barton, Geller, & Kenyon 2000). The samples in Fig. 16 are ordered from (a) to (e) by the level of interaction activity – from no interaction (NFGS field galaxies), to non-IR selected galaxy pairs, to luminous IR-selected galaxies, and to the most luminous IR-selected galaxies (1 Jy ULIRGs).

The fraction of starburst-AGN composite galaxies increases from the field galaxy sample (3.6%) → galaxy pair sample (22.8%) → SW01 galaxies (29.6%) → BGS galaxies (dominated by LIRGs) (37%) → 1 Jy ULIRGs (49.1%). This plot indicates that the stronger the interaction between galaxies is, the more likely they are to contain starburst-AGN composite galaxies.

Our new results offer some hope for resolving previous disputes concerning the evolution of starburst and AGN activity in gas-rich major mergers, in particular for ULIRGs. We have shown that a large fraction of ULIRGs are of composite starburst-AGN spectral type, with line ratios (or D_{AGN}) indicating an intermediate class between pure starbursts and pure AGN. Spectral classification as a function of merger evolution does not change abruptly from “pure” starburst into “pure” AGN. ULIRGs may spend a fairly large fraction of their merger history in a phase where starburst and AGN both make significant contributions to the EUV radiation. In luminous IR mergers, starburst-AGN composites appear to “bridge” the spectral evolution from pure starburst to AGN-dominated activity as the merger progresses. For ULIRGs, we have shown that an initial apparent decrease in starburst activity from the wide binary to close binary stage is accompanied by a rise in the starburst-AGN composites. Similarly, as the merger reaches its final stages, the fall in starburst-AGN composites is followed by a rise in Seyfert activity. These effects can be seen in Fig. 8, where the starburst-AGN composite activity peaks in the diffuse merger stage. We do not have sufficient data to determine whether a similar scenario occurs at the lower IR luminosities spanned by the BGS and SW01 samples ($L_{IR} < 10^{12} L_{\odot}$).

4.3. The Merger Scenario for LIRGs → ULIRGs

There is now substantial agreement that ULIRGs are triggered by major mergers of gas-rich spirals (see the review by Sanders & Mirabel 1996). In this merger scenario, the LIRG phase begins when tidal interactions between merging gas-rich disk galaxies initially trigger wide-spread starburst activity in one or both disks. As the merger progresses, gas is funneled towards the merger nucleus and activates nuclear starbursts and AGN, further increasing the IR luminosity. However, many questions still remain. The precise link between AGN fueling, the gas dynamics, and star formation either on a nuclear or a global scale is still poorly determined. The relative strength of starburst and AGN activity, particularly in the ULIRGs is still debated, and the question of whether the majority of LIRG mergers become ULIRGs has not been clearly addressed.

Our new results shown in Figs. 9-16 provide new insight into how starburst and AGN activity evolve during interaction/merger of IR-luminous galaxies.

For lower luminosity IR-galaxies ($L_{IR} < 10^{12} L_{\odot}$), Seyferts are rare ($D_{AGN} = 0.25 - 0.35$), and starbursts

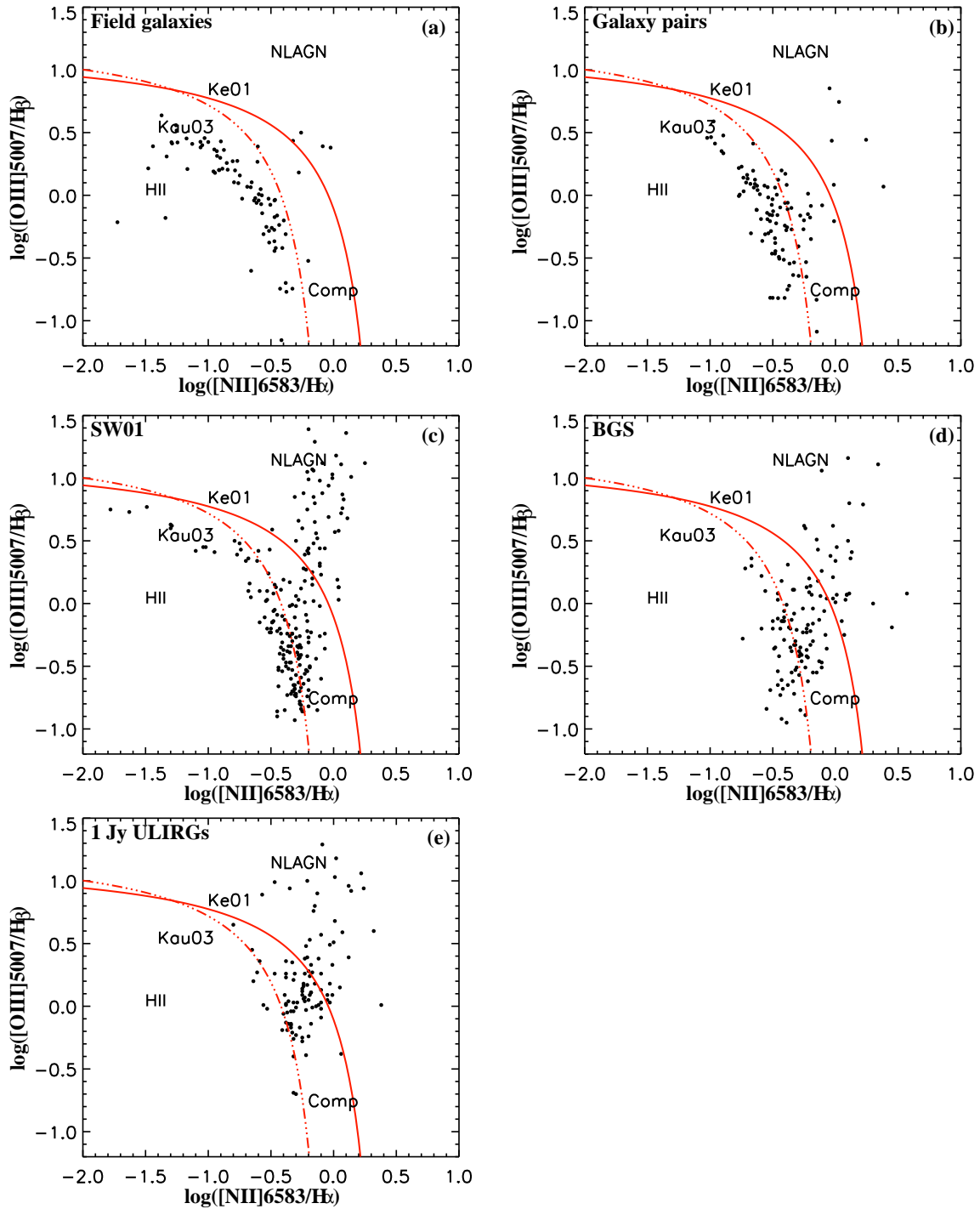


FIG. 16.— Composite galaxies on the “[N II] diagram” for different types of galaxy samples. (a) Field galaxy sample: NFGS (Jansen et al. 2000), (b) Galaxy pair sample: BGK00 (Barton, Geller, & Kenyon 2000), (c) SW01 sample, (d) BGS sample, (e) 1 Jy ULIRG sample.

strongly contribute to the EUV radiation field either as “pure” starbursts or as composites. The majority of lower luminosity LIRGs are wide or close pairs. These pairs may either evolve into the single merger stage without becoming ULIRGs, or they may enter the ULIRG phase during or shortly after the close pair stage. We consider both cases:

(1) Some lower luminosity IR galaxies ($L_{\text{IR}} < 10^{12}L_{\odot}$) may reach the final single merger stage without becoming ULIRGs. As these non-ULIRG galaxies evolve from the close pair to the single merger stage, the mean IR luminosity increases by $\sim 2\times$ (to $L_{\text{IR}} \sim 10^{11.5}L_{\odot}$), with only a relatively small rise in the mean value of $D_{\text{AGN}}(\sim 0.4)$. These results suggest that non-ULIRGs undergo a rise in starburst activity but only modest AGN growth as they evolve from the close pair to the single merger stage. Some of these lower luminosity single mergers may be the product of minor mergers of objects with mass ratios larger than 5:1 (Ishida 2004; Ishida et al. 2007).

(2) The lower luminosity pairs that may become ULIRGs are likely to be major mergers with mass ratios closer to unity (Ishida 2004; Ishida et al. 2007). In the ULIRG phase, the AGN contribution is elevated at all merger stages. We observe clear changes in the optical classification of ULIRGs as a function of merger stage. The diffuse merger stage (compared to the close binary stage) shows a dramatic increase in starburst-AGN composites (from $\sim 45\%$ to $\sim 80\%$). In the subsequent compact/old merger stages, the fraction of composite galaxies falls, and AGN dominate. The mean value of D_{AGN} rises (by ~ 0.22 dex – from 0.43 to 0.65), and the mean value of L_{IR} rises ($\sim 1.7\times$), along with the emergence of a substantial Seyfert 1 fraction ($\sim 25\%$). These results suggest that during the diffuse merger stage, the AGN becomes more powerful and increasingly visible via the optical emission-line ratios. Once the merged nucleus begins forming a core (compact merger stage) starburst activity may be subsiding (and possible dust obscuration clears) as AGN activity becomes prominent. We tentatively suggest that the dramatic increase in D_{AGN} and the emergence of a substantial population of Seyfert 1s (accompanied by a $\sim 2\times$ increase in L_{IR}) may signify a significant “blowout” phase, as ULIRGs transition to optical QSOs (e.g., Hopkins et al. 2005). A larger sample of ULIRGs is required to test this idea.

5. SUMMARY

We apply the new SDSS semi-empirical optical spectral classification scheme to three IR-selected galaxy samples – the 1 Jy ULIRG Sample, the *IRAS* Bright Galaxy Sample and the Southern Warm IR Galaxy Sample. Because the new classification scheme is substantially different from previous methods, the new scheme is used to yield insights into the relationship between starburst and AGN activity and merger progress. We utilize optical and near-IR images to determine the projected separation between pairs in our samples, and to classify the galaxies morphologically. The projected separation and morphological classification are used as relative tracers of merger progress. For each sample, we investigate how the optical classification and the relative AGN contribution, D_{AGN} , changes as a function of L_{IR} and merger progress.

We find that:

1. IR-luminous LINERs are rare; There are very few LINERs in the 1 Jy ULIRG, and the BGS and SW01 samples. The rarity of LINERs in the 1 Jy ULIRG and SW01 samples may be at least partly due to selection effects. Nearly all of the previously classified IR-luminous LINERs are starburst/AGN

composite galaxies in the Ke06 classification scheme.

2. The new classification scheme reveals a clear evolutionary scenario for ULIRGs from starburst-driven activity in the early merger stages, composite starburst-AGN activity intermediate merger stages to AGN-dominated emission at late merger stages. The fraction of composite galaxies rises from 45% to 80% between the wide binary and diffuse merger stages and appears to “bridge” pure starburst and Seyfert galaxies. Galaxies at the diffuse merger stage are key for future investigations into the relationship between starburst and AGN activity in ULIRGs.

3. We find that advanced mergers preferentially occur in ULIRG samples. We suggest that the transition into the ULIRG phase occurs close to or during the diffuse merger stage in which the nuclei of the two merging galaxies are coalescing.

4. At later merger stages in ULIRGs, when the single nucleus is forming a core, the fraction of pure-Seyfert objects rises dramatically. This stage corresponds to the highest L_{IR} in the 1 Jy ULIRG sample. At this stage, we propose that (a) starburst activity subsides, allowing the AGN to dominate the energy budget, and/or (b) dust obscuration surrounding the AGN clears, allowing the AGN radiation field to ionize the surrounding gas, and/or (c) AGN activity increases.

5. Seyfert 1s appear to occur only in the final “compact/old merging” stages of ULIRGs. A larger sample of Seyfert 1s is required to determine the significance of this result. If this result holds for larger samples, we hypothesize that a rise in Seyfert 1 galaxies at late merger stages may signify a significant “blowout” phase, as ULIRGs transition to optical QSOs.

6. There is no significant change in spectral types for the non-ULIRG BGS and SW01 samples.

Understanding the behavior of composite galaxies may help to build a more concrete picture of the merger process for all IR-luminous galaxies. Our future work includes integral field spectroscopy of composite galaxies and a detailed comparison between our results and the evolutionary merger models from numerical simulations Barnes (2004); Hopkins et al. (2005, 2006a,b, 2007, 2008).

We thank D.-C. Kim for providing the images for the 1 Jy ULIRG sample and Sturm, E. for his mid-infrared data. We also thank T. Heckman for helpful comments. We are grateful to the referee for some very good suggestions/comments that significantly improved this paper. This work has made use of the Digitized Sky Surveys (DSS) that were produced at the Space Telescope Science Institute, under US government grant NAG W-2166, and the NASA/IPAC Extragalactic Database (NED), which is operated by the Jet Propulsion Laboratory, California Institute of Technology. The 2MASS data were obtained from the NASA/IPAC Infrared Science Archive, which is operated by the Jet Propulsion Laboratory, California Institute of Technology, under contract with NASA.

APPENDIX

 D_{AGN} FROM DIFFERENT BPT DIAGRAMS

Theoretical models have shown that the distribution of galaxies on the BPT diagrams are mainly driven by variations of parameters such as metallicity, stellar age, ISM pressure and ionization parameter (Dopita et al. 2000; Kewley 2001; Groves, Dopita & Sutherland 2004; Dopita et al. 2006). The different sensitivity to these parameters of the four line ratios makes the three BPT diagrams distinct in distinguishing certain branches of galaxies.

Kewley et al. (2006) defined D_{AGN} on the [O I]/ $H\alpha$ diagram because the Seyfert and LINER branches are most clearly separated on the [O I]/ $H\alpha$ diagram. In this case, D_{AGN} can be defined separately for Seyferts and LINERs. The disadvantage of this diagram is that pure star-forming galaxies have to be removed first using the other two diagrams, because star-forming galaxies and starburst-AGN composites occupy similar regions on the [O I]/ $H\alpha$ diagram.

The advantage of the [N II]/ $H\alpha$ diagram is that the star-forming sequence is most tightly formed, giving a better contrast with the starburst-AGN branch. Also, [N II] has higher signal-to-noise than [O I]. However, in this diagram, Seyferts and LINERs can not be well separated. We define D_{AGN} on the [N II]/ $H\alpha$ diagram in Fig. 17: first, we empirically fit the SDSS star-forming sequence with a curve. Then, three points are chosen from the curve as “base points” (empty red circles in the lower left region in Fig. 17). Another three “peak points” (empty red circles in the upper right region in Fig. 17) are chosen from the upper right region of the diagram as $D_{\text{AGN}} = 1$. These points construct three “evolutionary line” intervals (line a, b, c in Fig. 17). We divide the intervals equally into 10 bins which define regions for different values of D_{AGN} , e.g., for the region below curve 0, $D_{\text{AGN}} = 0$; for the region above curve 0 and below curve 1, $D_{\text{AGN}} = 0.1, \dots$, and $D_{\text{AGN}} = 1$ for the region above curve 10. Note that D_{AGN} is defined differently from the “radial-arc” system used in Kewley et al. (2006), specifically for the [O I]/ $H\alpha$ diagram, because the starburst-AGN branch does not simply develop from one base point on the [N II]/ $H\alpha$ diagram.

We list the D_{AGN} defined on both diagrams in Tables 1-1. There is little difference in the two differently defined D_{AGN} , however, it is not meaningful to compare the absolute value of D_{AGN} . As emphasized in the text, only the relative value of D_{AGN} is useful. As an example, we show in Fig. 18 that our results in § 3.4 do not change when we apply the D_{AGN} defined on the [N II]/ $H\alpha$ diagram. Defining D_{AGN} on the [S II]/ $H\alpha$ diagram does not change in the results.

There is a good relation between D_{AGN} and spectral types: the mean value of D_{AGN} increases from star-forming galaxies, to starburst-AGN composites, and to Seyfert 2 and LINERs. Table 1 lists the spectral types and their corresponding mean and median D_{AGN} . The values are based on ~ 400 galaxies from the 1 Jy ULIRG, BGS and SW01 samples, as given in Table 1, 1 and 1. Star-forming galaxies have $D_{\text{AGN}} \leq 0.2$, starburst-AGN composites have a mean $D_{\text{AGN}} = 0.4(0.4)$, and Seyferts/LINERs have $D_{\text{AGN}} = 0.7(0.8)$. We assign $D_{\text{AGN}} = 1$ to Seyfert 1 objects since they are not included in the BPT diagrams and are almost certainly dominated by an AGN.

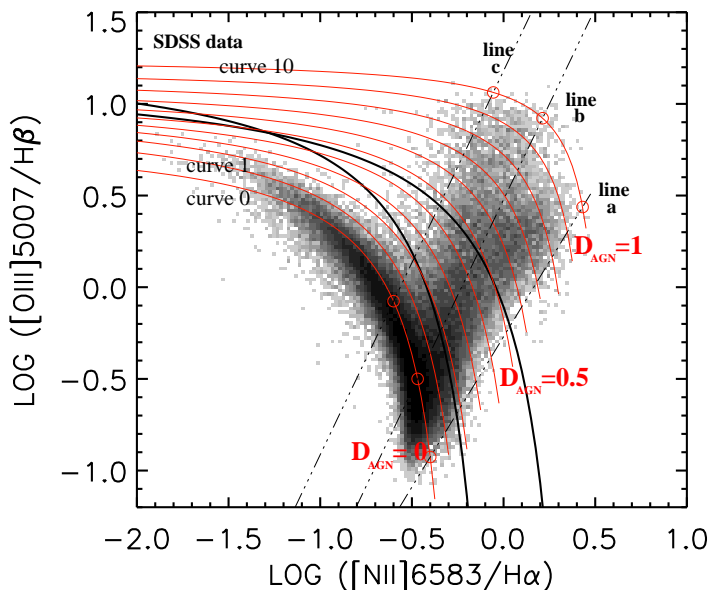


FIG. 17.— D_{AGN} defined on the “[N II]” diagram. “Base” and “peak” points are chosen to fit the outer boundary of the star-forming sequence and the $D_{\text{AGN}} = 1$ curve. The regions between the boundary and curve are then divided into 10 bins to define the value of D_{AGN} .

CLASSIFICATION CRITERIA AND “AMBIGUOUS” CLASS

In § 2.2, we use the 2-of-3 criterion to assign a class to our samples, based on agreement between two out of the three standard optical diagnostic diagrams. The 2-of-3 criterion has two advantages: (1) the final classification is less sensitive to low signal-to-noise in either [O I] or [S II] which may sometimes be weak, and (2) galaxies without [S II] or [O I] measurements can be

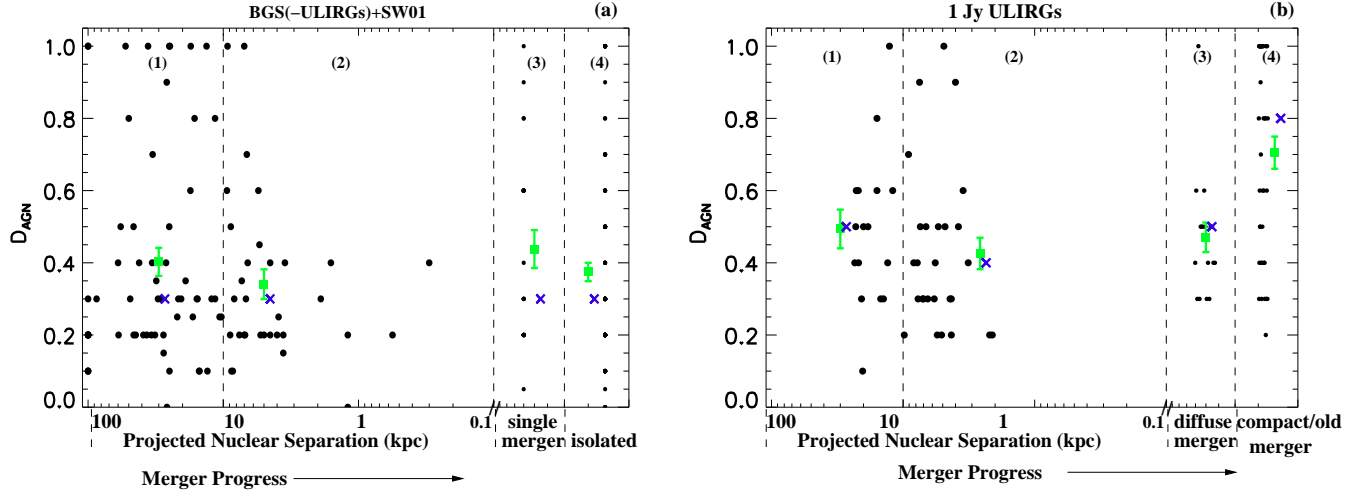


FIG. 18.— As in Fig. 12 and Fig. 13, but using D_{AGN} as defined on the $[\text{N II}]/\text{H}\alpha$ diagram.

assigned a class based on the remaining one or two diagnostic diagrams.

In Figure 19, we show the galaxies in the 3 samples classified using the 2-of-3 criterion on the BPT diagrams. As outlined in Kewley et al. (2006), the $[\text{N II}]/\text{H}\alpha$ line ratio is more sensitive to the presence of low-level AGN than $[\text{S II}]/\text{H}\alpha$ or $[\text{O I}]/\text{H}\alpha$ because $[\text{N II}]/\text{H}\alpha$ is more sensitive to metallicity. The $\log([\text{N II}]/\text{H}\alpha)$ line ratio is a linear function of the nebular metallicity until high metallicities where the $\log([\text{N II}]/\text{H}\alpha)$ ratio saturates. This saturation point causes the star-forming sequence to be almost vertical at $\log([\text{N II}]/\text{H}\alpha) = 0.5$. Any AGN contribution moves $[\text{N II}]/\text{H}\alpha$ above this saturation level, allowing the identification of galaxies with even small AGN contributions.

The $[\text{S II}]/\text{H}\alpha$ and $[\text{O I}]/\text{H}\alpha$ line ratios can not be used to distinguish composite galaxies from pure star-forming galaxies. In the $[\text{S II}]/\text{H}\alpha$ and $[\text{O I}]/\text{H}\alpha$ diagnostic diagrams, composite galaxies occupy a region that is degenerate with the star-forming galaxy sequence. This problem is caused by the relationship between $[\text{S II}]/\text{H}\alpha$ and $[\text{O I}]/\text{H}\alpha$ and metallicity. The AGN-starburst mixing sequence begins at the high metallicity end of the star-forming galaxy sequence. The $[\text{S II}]/\text{H}\alpha$ and $[\text{O I}]/\text{H}\alpha$ line ratios (unlike the $[\text{N II}]/\text{H}\alpha$ ratio) are double-valued with metallicity over the range of observed $[\text{S II}]/\text{H}\alpha$ and $[\text{O I}]/\text{H}\alpha$ ratios in nearby galaxies. The highest metallicity star-forming galaxies occur at low $[\text{S II}]/\text{H}\alpha$ and $[\text{O I}]/\text{H}\alpha$ ratios ($\log([\text{S II}]/\text{H}\alpha) = -0.6$ to -0.9 , and $\log([\text{O I}]/\text{H}\alpha) = -2.0$ to -1.4) (see Figures in Dopita et al. 2000; Kewley 2001). Therefore, a large AGN contribution ($\sim 40 - 50\%$) is required for a composite galaxy to rise above the star-forming galaxy sequence.

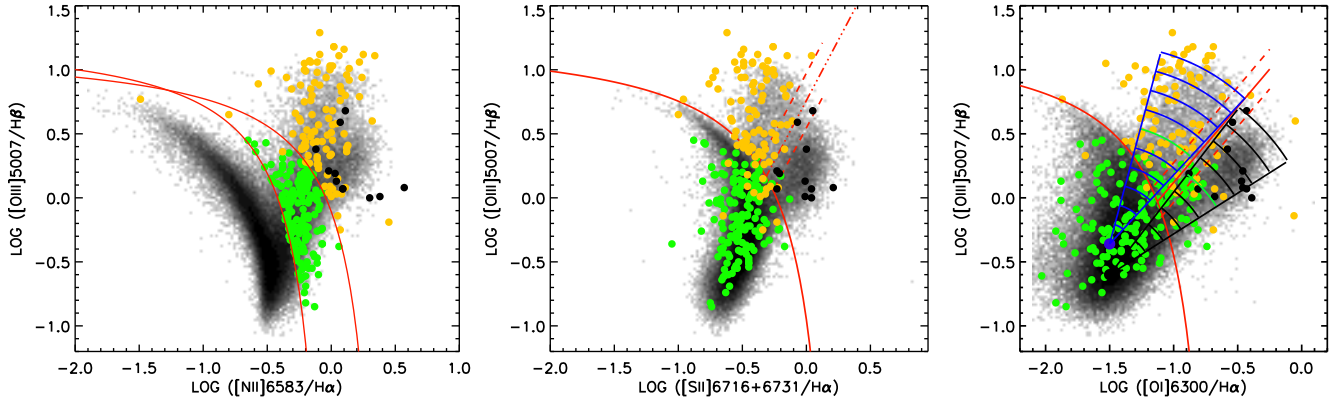


FIG. 19.— Classified galaxies in the 3 samples using the 2-of-3 criterion. Green: composites. Orange: Seyfert2, Black: LINERs. Solid red lines are the new classification boundaries as in Fig. 1. Wedges on the $[\text{O I}]/\text{H}\alpha$ diagram are used to derive D_{AGN} as described in Fig. 3

The 3-of-3 criterion is a more stringent method of classification that is based on all three diagnostic diagrams. This method allows ambiguous galaxies to be classified as those galaxies that have one classification in one or two diagrams and a different classification in the remaining diagram(s). The 3-of-3 criterion is suitable for galaxies with high S/N spectra where all five diagnostic emission-lines have $S/N > 3$ (e.g., Kewley et al. 2006). Samples with lower S/N emission-lines may contain a large fraction of ambiguous galaxies if the 3-of-3 criterion is applied.

According to the 3-of-3 scheme, the 1 Jy ULIRGs contain 4 (4.0%) HII-region galaxies, 18 (18%) starburst-AGN composites, 23 (23%) Seyfert 2, 10 (10%) Seyfert 1, and 3 (3%) LINERs. The remaining 41 (41%) galaxies are ambiguous, illustrating the effect of low S/N for the $[\text{S II}]$ and/or $[\text{O I}]$ emission-lines in this sample.

For the LIRGs in the BGS sample, a total of 74 single nucleus galaxies have measured spectra on all three diagrams. Using the 3-of-3 criterion, 22 (29.7%) are HII-region galaxies, 19 (25.7%) are starburst-AGN composites, 8 (10.8%) are Seyfert 2, 1 galaxy (1.4%) is a Seyfert 1, and 5 (6.7%) are LINERs. The remaining 19 (25.7%) galaxies are ambiguous.

For the SW01 sample, a total of 175 single nucleus objects that have measured emission line fluxes with $S/N > 3\sigma$. The majority of the sample has $S/N > 8\sigma$ for all five diagnostic lines. In the 3-of-3 scheme, we obtain 70 (40.0%) HII-region galaxies, 48 (27.4%) starburst-AGN composites, 33 (18.9%) Seyfert 2, 10 (5.7%) Seyfert 1, and 2 (1.1%) LINERs. The remaining 12 (6.8%) galaxies are ambiguous.

With the 3-of-3 criterion, we obtain a large fraction of ambiguous galaxies in the ULIRGs and BGS samples (41% and 25.7% respectively), while the fraction of ambiguous galaxies in the SW01 sample is relatively small (7%). The fraction of ambiguous galaxies in the SW01 sample is consistent with the fraction of ambiguous galaxies in the Sloan Digital Sky Survey where a $S/N > 3$ cut has been applied.

Among the ambiguous galaxies in the ULIRGs, 68% are ambiguous between composites and Seyferts/LINERs, i.e., they lie within the composite galaxy region on the $[N II]/H\alpha$ diagram, but lie above the Ke01 line on either (or both) the $[S II]/H\alpha$ or the $[O I]/H\alpha$ diagram. Many of these galaxies lie within the ± 0.1 dex error region of either (or both) the $[S II]/H\alpha$ or the $[O I]/H\alpha$ classification line and hence their classification with these diagram(s) is uncertain. Hill et al. (1999) and Hill et al. (2001) investigate ambiguous galaxies using near-infrared spectroscopy and radio observations. They conclude that ambiguous galaxies are starburst-AGN composites. Spitzer spectroscopy of our ambiguous 1 Jy ULIRGs supports this conclusion; 5/6 of the ULIRG ambiguous galaxies observed by Imanishi et al. (2007) have evidence (either strong or tentative) of a buried AGN. Our results are unchanged if the 3-of-3 criterion is applied and if the ambiguous galaxies found using this criterion are starburst-AGN composites.

DOUBLE NUCLEI GALAXIES WITH DIFFERENT SPECTRAL TYPES

There are 23 double nuclei galaxies in the BGS. Of these, 13 have the same spectral type for the two nuclei (7 HII, 6 composites). For the remaining 10 galaxies, 5 have classes available only for one nucleus (4 HII, 1 composite); the remaining 5 have different spectral types for each nucleus (1 composite/HII, 2 composite/Seyfert 2, and 2 HII/Seyfert 2). There are 9 double nuclei galaxies in the 1Jy sample. A total of 4 of these double nuclei galaxies have the same spectral type for each nucleus (composite). The remaining 5/9 1 Jy ULIRGs all have a composite class for one nucleus (3 composite/HII, 2 composite/Seyfert 2). There are 17 double nuclei galaxies in the SW01 sample. A total of 13 of these double nuclei galaxies have the same spectral type (8 HII, 3 composite, 2 Seyfert 2). Only 4 of the 17 double nuclei galaxies in SW01 have different spectral types (1 composite/LINER, 2 composite/HII, and 1 HII/Seyfert 2).

There are only 14 objects across all three samples that have different spectral types for each nucleus. We estimate the ranges of uncertainty in our composite classification by first assigning all the double nuclei galaxies with different spectral types as composites in order to derive an upper limit for the “composite” fraction. We next assign all of the double nuclei galaxies with different spectral types the alternative types listed above to derive a lower limit of the “composite” fraction. The change in the fraction (shown as dashed lines in Figures 8 - 11) of the composite galaxies indicates the range of uncertainty introduced by these 14 objects.

REFERENCES

- Armus, L., Heckman, T. M., & Miley, G. K. 1990, *ApJ*, 364, 471
- Baldwin, J., Phillips, M., & Terlevich, R. 1981, *PASP*, 93, 5 (BPT)
- Barnes, J. E., & Hernquist, L. E. 1996, *ApJ*, 471, 115
1992, *ARA&A*, 30, 705
- Barnes, J. E. 2004, *MNRAS*, 350, 798
- Barth, A. J. 2002, in *Issues in Unification of AGNs*, ed. R. Maiolino, A. Marconi, & N. Nagar (San Francisco: ASP), 147
- Barton, E. J., Geller, M. J., & Kenyon, S. J. 2000, *ApJ*, 530, 660
- Becklin, E. E., Frogel, J. A., Kleinmann, D. E., Neugebauer, G., Ney, E. P., & Strecker, D. W. 1971, *ApJ*, 170L, 15B
- Becklin, E. E., & Neugebauer, G. 1972, *BAAS*, 4, 224
- Bonatto, C. J., & Pastoriza, M. G. 1997, *ApJ*, 486, 132
- Borne, K. D., Bushouse, H., Lucas, R. A., & Colina, L. 2000, *ApJ*, 529, L77
- Bushouse, H. A. 1987, *ApJ*, 320, 49
- Clements, D. L., Sutherland, W. J., McMahon, R. G., & Saunders, W. 1996, *MNRAS*, 279, 477
- Clements, D. L., & Baker, A. C. 1996, *A&A*, 314, 5
- Clements, D. L., McDowell, J. C., Shaked, S., Baker, A. C., Borne, K., Colina, L., Lamb, S. A., & Mundell, C. 2002, *ApJ*, 581, 974
- Dasyra, K. M., et al. 2006, *ApJ*, 638, 745
- Denicoló, G., Terlevich, R., & Terlevich, E. 2002, *MNRAS*, 330, 69
- Dopita, M. A., Kewley, L. J., Heisler, C. A., & Sutherland, R. S. 2000, *ApJ*, 542, 224
- Dopita, M. A., et al. 2006, *ApJS*, 167, 177
- Downes, D., & Eckart, A. 2007, *A&A*, 468, 57
- Farrah, D., et al. 2001, *MNRAS*, 326, 1333
- Farrah, D., Afonso, J., Efstathiou, A., Rowan-Robinson, M., Fox, M., & Clements, D. 2003, *MNRAS*, 343, 585
- Farrah, D., et al. 2007, *ApJ*, 667, 149
- Filippenko, A., & Sargent, W. L. 1985, *ApJS*, 57, 503
- Garcia, A. M. 1993, *A&AS*, 100, 47
- Genzel, R., et al. 1998, *ApJ*, 498, 579
- Goldader, J. D., Joseph, R. D., Doyon, R., & Sanders, D. B. 1995, *ApJ*, 444, 97
- Goto T. 2005, *MNRAS*, 360, 322
- Groves, B. A., Dopita, M. A., & Sutherland, R. S. 2004, *ApJS*, 153, 9
- Groves, B. A., Heckman, T. M., & Kauffmann, G. 2006, *MNRAS*, 371, 1559
- Giuricin, M., Mardirossian, F., Mezzetti, M. 1995, *ApJ*, 446, 550
- Haas, M., Seibenmorgen, R., Pantin, E., Horst, H., Smette, A., Kaufl, H.-U., Lagage, P.-O., & Chini, R. 2007, *A&A*, 473, 369
- Heckman, T. M., Balick, B., & Crane, P. C. 1980, *A&AS*, 40, 295
- Heckman, T., Timothy, M., Armus, L., Miley, G., K. 1987, *AJ*, 93, 276
- Heckman, T. 1995, *ApJ*, 446, 101
- Heisler, C. A., & Vader, J. P. 1995, *A&A*, 110, 87
- Hill, T. L., Heisler, C. A., Sutherland, R. P., & Hunstead, R. W. 1999, *AJ*, 121, 128
- Hill, T. L., Heisler, C. A., Norris, R. P., Reynolds, J. E., & Hunstead, R. W. 2001, *AJ*, 121, 128
- Ho, L. C. 1999, *Adv. Space Res.*, 23 (5-6), 813
- Hopkins, P. F., Hernquist, L., Cox, T. J., Matieo, T. D., Martini, P., Robertson, B., & Springel, V. 2005, *ApJ*, 630, 705
- Hopkins, P. F., Somerville, R. S., Hernquist, L., Cox, T. J., Robertson, B., & Li, Y. 2006, *ApJ*, 625, 864
- Hopkins, P. F., Hernquist, L., Cox, T. J., Matieo, T. D., Robertson, B., & Springel, V. 2006, *ApJS*, 163, 1
- Hopkins, P. F., Bundy, K., Hernquist, L., & Ellis, R. S. 2007, *ApJ*, 659, 976
- Hopkins, P. F., Hernquist, L., Cox, T. J., & Keres, D. 2008, *ApJS*, 175, 356
- Imanishi, M., Dudley, C., & Maloney, P. R. 2006, *ApJ*, 637, 114
- Imanishi, M., Dudley, C., Maiolino, R., Maloney, P. R., Nakagawa, T., & Risaliti, G. 2007, *ApJS*, 171, 72
- Iono, D., et al. 2007, *ApJ*, 659, 283
- Ishida, C. M. 2004, Ph.D. Thesis, University of Hawaii
- Ishida, C. M., et al. 2007, to be submitted to *ApJS*
- Iwasawa, K., Sanders, D. B., Evans, A. S., Trentham, N., Miniutti, G., & Spoon, H., W. 2005, *MNRAS*, 357, 565
- Jansen, R. A., Franx, M., Fabricant, D., & Caldwell, N. 2000, *ApJS*, 126, 271
- Joseph, R. D. 1999, *A&SS*, 266, 321
- Kauffmann, G., et al. 2003, *MNRAS*, 346, 1055
- Kawakatu, N., Anabuki, N., Nagao, T., Umemura, M., & Nakagawa, T. 2006, *ApJ*, 637, 104
- Kennicutt, R. C., et al. 1987, *AJ*, 93, 1011
- Kennicutt, R. C. & Keel, W. C. 1984, *ApJ*, 279, 5
- Keel, W. C. 1983, *ApJ*, 269, 466
- Kewley, L. J. 2001, Ph.D thesis
- Kewley, L. J., Heisler, C. A., & Dopita, M. A. 2001a, *ApJS*, 132, 37
- Kewley, L. J., Dopita, M. A., Sutherland, R. S., Heisler, C. A., & Trevena, J., 2001b, *ApJ*, 556, 121
- Kewley, L. J., & Dopita, M. A. 2002, *ApJS*, 142, 35
- Kewley, L. J., Groves, B., Kauffmann, G., & Heckman, T. 2006, *MNRAS*, 372, 961
- Kim, D.-C. 1995, The IRAS 1 Jy survey of ultraluminous infrared galaxies, Ph.D. thesis, Univ.Hawaii
- Kim, D.-C., Sanders, D. B., Veilleux, S., Mazzarella, J. M., & Soifer, B. T. 1995, *ApJS*, 98, 129
- Kim, D.-C., & Sanders, D. B. 1998, *ApJS*, 119, 41
- Kim, D. C., Veilleux, S., & Sanders, D. B. 2002, *ApJS*, 143, 277
- Kleinmann, D. E., & Low, F. J. 1970, *ApJ*, 159, 165
- Kleinmann, D. E., & Low, F. J. 1970, *ApJ*, 161, 203
- Komossa, S., Burwitz, V., Hasinger, G., Perdehl, P., Kaastra, J. S., Ikebe, Y. 2003, *ApJ*, 582, L15
- Lipari, S., Terlevich, R., Díaz, R. J., Taniguchi, Y., Zheng, W., Tsvetanov, Z., Carranza, G., & Dottori, H. 2003, *MNRAS*, 340, 289
- Lira, P., Ward, M. J., Zezas, A., & Murray, S. S. 2002, *MNRAS*, 333, 709
- Liu, C. T., & Kennicutt, R. C. 1995, *ApJS*, 100, 325
- Low, F. J., & Kleinmann, D. E. 1968, *AJ*, 73, 868
- Maiolino, R., Ruiz, M., Rieke, G. H., & Keller, L. D. 1995, *ApJ*, 446, 561
- Maloney, P., Hollenbach, D., & Tielens, A. G. G. M. 1996, *ApJ*, 466, 561
- McDowell, J. C., et al. 2003, *ApJ*, 591, 154
- Mihos, J. C., & Hernquist, L. 1994, *ApJ*, 431, L9
- Nardini, E., et al. 2008, *MNRAS Letters*, accepted/arXiv:0801.4304
- Neugebauer, G., et al. 1984, *ApJ*, 278, L1
- Osterbrock, D. E., & de Robertis, M. M. 1985, *PASP*, 97, 1129
- Pettini, M. & Pagel, B. E. J. 2004, *MNRAS*, 348, L59
- Ptak A., Heckman T., Levenson N. A., Weaver K., Strickland D. 2003, *ApJ*, 592, 782
- Quataert, E. et al., Probing the Physics of Active Galactic Nuclei, ASP conf. Ser. 224
- Rieke, G. H., & Low, F. J. 1972, *ApJ*, 176, 95
- Sanders, D. B. 1999, *A&SS*, 266, 331
- Sanders, D. B., Soifer, B. T., Elias, J. H., Madore, B. F., Matthews, K., Neugebauer, G., & Scoville, N. Z. 1988a, *ApJ*, 325, 74
- Sanders, D. B., Soifer, B. T., Elias, J. H., Neugebauer, G., & Matthews, K. 1988b, *ApJ*, 328, L35
- Sanders, D. B., Egami, E., Lipari, S., Mirabel, I. F., & Soifer, B. T. 1995, *AJ*, 110, 1993
- Sanders, D. B., & Mirabel, I. F. 1996, *ARA&A*, 34, 725
- Soifer, B. T., Sanders, D. B., Neugebauer, G., Danielson, G. E., Lonsdale, C. J., Madore, B. F., & Persson, S. E. 1986, *ApJ*, 303, L41
- Soifer, B. T., Sanders, D. B., Madore, B. F., Neugebauer, G., Danielson, G. E., et al. 1987, *ApJ*, 320, 238
- Soifer, B. T., Boehmer, L., Neugebauer, G., & Sanders, D. B. 1989, *AJ*, 98, 766
- Stacy, H. T., Young, A. J., Sanders, D. B., & Nagar, N. M. 2005, *ApJ*, 633, 664
- Strauss, M. A., Huchra, J. P., Davis, M., Yahil, A., Fisher, K. B., & Tonry, J. 1992, *ApJS*, 83, 29
- Sturm, E., et al. 2006, *ApJ*, 653: L13
- Taniguchi, Y., Ikeuchi, S., & Shioya, Y. 1999, *ApJ*, 514, L9
- Tecza, M., Genzel, R., Tacconi, L. J., Anders, S., Tacconi-Garman, L. E., & Thatte, N. 2000, *ApJ*, 537, 178
- Toomre, A., & Toomre, J. 1972, *ApJ*, 178, 623s
- Tran, Q. D., et al. 2001, *ApJ*, 552, 527
- Veilleux, S., & Osterbrock, D. E. 1987, *ApJS*, 63, 295
- Veilleux, S., Kim, D. C., Sanders, D. B., Mazzarella, J. M., & Soifer, B. T. 1995, *ApJS*, 98, 171
- Veilleux, S., Kim, D. C., & Sanders, D. B. 1999, *ApJ*, 522, 113
- Veilleux, S., Kim, D. C., & Sanders, D. B. 2002, *ApJS*, 143, 315
- Vorontsov-Velyaminov, B., & Arhipova, V. P. 1868, *Morphological Catalogue of Galaxies Volume IV* (Moscow: Moscow State University)
- Weedman, D. W. 1983, *ApJ*, 266, 479
- Zauderer, B. A., Veilleux, S., & Yee, H. K. C. 2007, *ApJ*, 659, 1096

TABLE 1
SPECTRAL CLASSIFICATION RESULT FOR THE 1 JY ULIRG SAMPLE

Name IRAS FSC (1)	Spectral Type					D_{AGN} (7)	Morphology Class (8)	$\log(L_{\text{IR}}/L_{\odot})$ (9)
	[NII] (2)	[SII] (3)	[OI] (4)	Adopt (5)	"VO87" (6)			
00091-0738	cp	H	H	cp	H:	0.1 (0.2)	b	12.19
00188-0856	S2	H	S2	S2:	L	0.7(0.8)	e	12.33
00397-1312	cp	H	H	cp	H	0.4 (0.3)	e	12.90
00456-2904	cp	H	H	cp	H	0.2 (0.3)	a	12.12
00482-2721	cp	H:	L	cp:	L:	0.8 (0.5)	b	12.00
01004-2237	cp	S2	S2	S2:	H:	0.7 (0.4)	e	12.24
01166-0844	H::	H	...	H:	H:	0 (0.2)	b	12.03
01199-2307	H:	H:	S2:	H:	H:	0.6 (1)	a	12.26
01298-0744	cp	H	L	cp:	H:	0.6 (0.3)	d	12.27
01355-1814	cp	H	H	cp	H	0.3 (0.3)	b	12.39
01569-2939	cp	H	S2	cp:	H:	0.6 (0.4)	c	12.15
01572+0009(MRK1014)	S1	S1	1 (1)	d	12.53
02411+0353:main	cp	H	H	cp	H	0.3 (0.3)	b	12.19
02411+0353:E	H	H	H	H	H	0 (0.4)	b	...
02411+0353:W	H	H	H	H	H	0 (0.2)	b	...
03209-0806	cp	H	H:	cp	H:	0.4 (0.4)	d	12.191
03250+1606	cp	H	S2	cp:	L	0.6 (0.5)	d	12.06
Z03521+0028	S2::	S2:	S2:	S2	L	0.6 (0.6)	b	12.45
04074-2801	L:	L	L	L	L	0.9 (0.6)	c	12.14
04103-2838	S2	H	S2	S2:	L:	0.7 (0.6)	d	12.15
05020-2941	cp::	H:	S2:	cp:	L:	0.4 (0.3)	c	12.28
05024-1941	S2::	S2:	S2:	S2	S2	0.9 (1)	c	12.43
05156-3024	S2	S2	S2:	S2	S2	1 (1)	d	12.20
05189-2524	S2	S2	S2	S2	S2	1 (1)	d	12.07
07599+6508	S1	S1	1 (1)	d	12.46
08201+2801	cp	H	H	cp	H	0.3 (0.3)	c	12.23
08559+1053	S2	S2	S2	S2	S2	0.8 (0.8)	d	12.16
08572+3915:NW	cp	S2	S2	S2:	L:	0.6 (0.4)	b	12.11
08572+3915:SE	S2	S2	H	S2:	L:	0.5(0.7)	b	...
09039+0503	cp	H	L	cp:	L	0.5 (0.5)	c	12.07
09116+0334	S2::	H	S2	S2:	L:	0.6 (0.6)	a	12.11
09463+8141	S2::	L:	S2:	S2:	L	0.7 (0.5)	c	12.29
09539+0857	S2	S2	L	S2:	L	0.8 (0.6)	e	12.03
10091+4704	cp	L	L	L:	L:	0.5 (0.5)	c	12.67
10190+1322	H	H	H	H	H	0 (0.2)	b	12.00
10378+1108	S2	H:	S2	S2:	L	0.6 (0.6)	d	12.26
10485-1447	S2::	H:	S2:	S2:	L:	0.8 (0.5)	a	12.17
10494+4424	cp	H	L	cp:	L	0.6 (0.4)	d	12.13
10594+3818	cp:	H:	H:	cp	H	0.3 (0.3)	b	12.24
11028+3130	cp	H	L	cp:	L	0.5 (0.6)	c	12.32
11095-0238	cp	H	L	cp:	L	0.6 (0.4)	d	12.20
11119+3257	S1	S1	1 (1)	d	12.58
11130-2659	cp::	H:	L:	cp:	L	0.7 (0.5)	c	12.05
11180+1623	cp:	H:	L:	cp:	L:	0.5 (0.4)	a	12.24
11223-1244	S2	S2	S2	S2	S2	1 (1)	a	12.59
11387+4116	S2	H	H	H:	H:	0.4 (0.5)	e	12.18
11506+1331	cp	H	L	cp:	H:	0.6(0.3)	d	12.28
11582+3020	cp	H	L	cp:	L	0.6 (0.5)	e	12.56
Z11598-0112	S1	S1	1 (1)	d	12.43
12032+1707	S2	H	S2	S2:	L	0.7 (0.6)	d	12.57
12072-0444	S2	S2	S2	S2	S2	0.9 (0.8)	d	12.35
12112+0305	S2	S2	S2	S2	L	0.7 (0.5)	b	12.28
12127-1412	S2::	H:	H:	H:	L:	0.4 (0.6)	a	12.10
12265+0219(3C273)	S1	S1	1 (1)	d	12.73
12359-0725:N	cp	H	L	cp:	L	0.7 (0.5)	a	12.11
12359-0725:S	H	H	H	H	H	0 (0.2)	a	...
12447+3721	cp:	H:	H:	cp	H	0.5 (0.3)	c	12.06
12540+5708(MRK0231)	S1	S1	1 (1)	d	12.50
13106-0922	cp	H	L	cp:	L:	0.7 (0.4)	c	12.32
13218+0552	S1	S1	1(1)	e	12.63
13305-1739	S2:	S2:	S2:	S2	S2	1 (0.9)	e	12.21
13335-2612	cp	H	S	cp:	L:	0.5 (0.4)	b	12.06
13342+3932	S1	S1	1 (1)	d	12.37
13428+5608(MRK0273)	S2	S2	S2	S2	S2	0.8 (0.8)	d	12.10
13443+0802:NE	cp	H:	H	cp	H	0.2 (0.3)	tpl	12.15
13443+0802:SW	S2	S2:	S2	S2	S2	1 (1)	tpl	...
13451+1232	S2	S2	S2	S2	S2	1(0.9)	b	12.28
13454-2956	S2	S2	S2	S2	S2	0.8 (0.8)	a	12.21
13469+5833	cp:	H:	H:	cp	H	0.1 (0.3)	b	12.15
13509+0442	cp	H:	H	cp	H	0.4 (0.2)	d	12.27
13539+2920	cp	H	H	cp	H:	0.5 (0.3)	b	12.00
14053-1958	L::	L:	L:	L	S2	1 (0.8)	b	12.12
14060+2919	cp	H	H	cp	H	0.2 (0.3)	c	12.03

TABLE 1 — *Continued*

Name IRAS FSC (1)	Spectral Type					D_{AGN} (7)	Morphology Class (8)	$\log(L_{\text{IR}}/L_{\odot})$ (9)
	[NII] (2)	[SII] (3)	[OI] (4)	Adopt (5)	“VO87” (6)			
14070+0525	S2	S2	S2	S2	S2	0.8 (0.7)	e	12.76
14121–0126	S2	H	S2	S2:	L	0.7 (0.7)	b	12.23
14202+2615	cp	H	H	cp	H	0.2 (0.3)	a	12.39
14252–1550	cp::	H	H	cp	L:	0.5 (0.4)	b	12.15
14348–1447:SW	cp	S2	L	cp::	L	0.7 (0.5)	b	12.28
14348–1447:NE	cp	H	L	cp:	L	0.6 (0.5)	b	...
14394+5332	S2	S2	L	S2:	S2	0.9 (0.7)	tpl	12.04
15001+1433	S2	S2	S2	S2	S2	0.7 (0.6)	tpl	12.38
15043+5754	H	H	H	H	H	0 (0.2)	b	12.05
15130–1958	S2	S2	S2	S2	S2	1 (1)	d	12.09
15206+3342	cp	H	H	cp	H	0.6 (0.3)	d	12.18
15225+2350	cp	H	S2	cp:	H:	0.6 (0.5)	a	12.10
15327+2340(Arp220)	L	L	L	L	L	0.7 (0.9)	b	12.17
15462–0450	S1	S1	1 (1)	d	12.16
16090–0139	cp	H	H	cp	L:	0.5 (0.5)	c	12.49
16156+0146	S2	S2:	S2	S2	S2	1 (1)	b	12.04
16300+1558	cp	H	L	cp:	L	0.6 (0.4)	e	12.63
16333+4630	cp	H	S2	cp:	L	0.5 (0.4)	a	12.35
16468+5200:W	cp	H	H	cp	L:	0.2 (0.4)	b	12.02
16468+5200:E	cp	L	H	cp:	L	0.4 (0.4)	b	...
16474+3430	cp	H	H	cp	H:	0.4 (0.3)	b	12.11
16487+5447	cp	H	S2	cp:	L:	0.5 (0.5)	b	12.12
17028+5817:W	cp	H	H	cp	L:	0.6 (0.4)	a	12.10
17028+5817:E	H	H	H	H	H	0 (0.1)	a	...
17044+6720	S2	S2	S2	S2	L	0.7 (0.6)	d	12.13
17068+4027	cp	H	H	cp	H	0.5 (0.3)	tpl	12.30
17179+5444	S2	S2	S2	S2	S2	1 (1)	d	12.20
20414–1651	cp	H	L	cp:	H:	0.5 (0.3)	d	12.14
21208–0519:N	cp	H:	H	cp	H	0.2 (0.3)	a	12.01
21208–0519:S	cp	H:	H	cp	H:	0.4 (0.4)	a	...
21219–1757	S1	S1	1 (1)	e	12.06
21329–2346	cp	H	L	cp:	L	0.5 (0.4)	d	12.09
21477+0502	cp	H:	L	cp:	L:	0.6 (0.4)	tpl	12.24
22088–1831	H	H:	H:	H	H:	0 (0.2)	b	12.31
22206–2715	cp	H	L	cp:	H:	0.5 (0.3)	b	12.19
22491–1808	H	H	H	H	H	0 (0.2)	b	12.09
22541+0833:NW	cp	L:	H	cp:	L:	0.4 (0.5)	a	12.23
22541+0833:SE	S2:	... (...)	a	...
23060+0505	S2	S2	S2:	S2	S2	0.9 (0.8)	d	12.44
23129+2548	cp::	H	L:	cp:	L:	0.5 (0.4)	c	12.38
23233+2817	S2	S2	S2	S2	S2	1 (1)	iso	12.00
23234+0946	cp	H	L:	cp:	L	0.6 (0.5)	b	12.05
23327+2913	S2	H	S2:	S2:	L:	0.6 (0.6)	a	12.06
23389+0300	S2:	S2:	L:	S2:	S2	1 (1)	b	12.09
23498+2423	S2	S2	S2:	S2	S2	0.9 (1)	a	12.40

NOTE. — Col. (1): Galaxy Name. Col. (2) to Col. (4)-Optical spectral types derived in this work from the [N II] $\lambda 6583$, [S II] $\lambda\lambda 6716, 6731$, and [O I] $\lambda 6300$ diagrams respectively. The typical uncertainty on the emission-line ratios is $\sim 10\%$; colons in Col. (3) and Col. (4) indicate larger uncertainty of the line ratios of $\sim 25\%$ for [S II]/ $H\alpha$ and [O I]/ $H\alpha$, respectively; double colons in Col. (2) indicate larger uncertainty of the line ratios of $\sim 25\%$ for [O III]/ $H\beta$. Col. (5) is the adopted spectral type using the 2-of-3 scheme; single colons indicate the object does not have the same spectral type in all 3 diagrams, i.e., the ambiguous class. Double colons means the classification does not agree on any of the diagrams, the classification in those rare cases is highly uncertain. For comparison, Col. (6) lists the VO87 classification results (Veilleux et al. 1999). Symbols: H = star-forming galaxies, L = LINERs, S2 = Seyfert 2 galaxies, S1 = Seyfert 1 galaxies, cp = starburst-AGN composite galaxies. Col. (7): D_{AGN} defined on the [O I]/ $H\alpha$ diagram, for comparison, in the bracket we also list the D_{AGN} derived from the [N II]/ $H\alpha$ diagram (see Appendix A). Col. (8): Morphology class as adopted from Veilleux et al. (2002). a: wide binary; b: close binary; c: diffuse merger; d: compact merger; e: old merger; tpl: triple mergers; iso: isolated. Col.(9): $\log(L_{\text{IR}}/L_{\odot})$, data from Veilleux et al. (1999).

TABLE 2
SPECTRAL CLASSIFICATION RESULT AND MORPHOLOGY FOR THE IRAS BGS
SAMPLE

Name (1)	Spectral Type					D_{AGN} (7)	n_s kpc (8)	"reference" (9)	Morphology Class (10)	$\log(L_{IR}/L_{\odot})$ (11)
	[NII] (2)	[SII] (3)	[OI] (4)	Adopt (5)	"VO87" (6)					
NGC 23	cp	H	H	cp	H	0.2(0.3)	-2	2MASS, DSS	iso	11.05
NGC 34	S2	S2	S2	S2	S2	0.7(0.8)	-1	2MASS, DSS	cde	11.41
MCG-02-01-051:S	H:	H	H	H	H	0(0.2)	27.7	2MASS	a	11.32
MCG-02-01-051:N	H	H	H	H	H	0(0.1)	27.7	2MASS	a	...
NGC 232	cp	H	H	cp	H:	0.4(0.5)	8.8	2MASS	b	11.30
UGC 556	cp	H	L	cp:	L	0.5(0.3)	-2	2MASS, DSS	iso	10.82
IC1623:N	H	H	H	H	H	0(0.2)	5.3	2MASS	b	11.54
IC1623:SE	H	H	H	H	H	0(0.2)	5.3	2MASS	b	...
MCG-03-04-014	cp	H	H	cp	H	0.1(0.2)	-2	2MASS, DSS	iso	11.58
MCG+02-04-025	H	H	H	H	H	0(0.2)	-1	2MASS, DSS	cde	11.63
UGC903	cp	H	H	cp	H:	0.2(0.3)	-2	2MASS, DSS	iso	10.37
NGC520	10.88
IR01364-1042	L:	L:	L:	L	L	0.8(0.6)	-1	2MASS, DSS	cde	11.76
NGC660	S2	S2	S2	S2	L	0.6(0.7)	-2	2MASS, DSS	iso	10.47
IIIzw 35:S	S2::	H	S2	S2:	L	0.7(0.6)	...	2MASS, DSS	...	11.54
IIIzs 35:N	H	H	H	H	H	0(0.1)	...	2MASS, DSS
NGC695	H	H	H	H	H	0(0.2)	-2	2MASS, DSS	iso	11.64
NGC873	H	H	H	H	H	0(0.2)	-2	2MASS, DSS	iso	10.60
NGC1050	cp	H	H	cp	H	0.1(0.3)	-2	2MASS, DSS	iso	10.72
NGC1056	H	H	H	H	H	0(0.2)	-2	2MASS, DSS	iso	9.92
NGC1068	S2:	S2:	S2:	S2	S2	1(1)	-2	2MASS, DSS	iso	11.27
NGC1083	H	H	H	H	H	0(0.2)	-2	2MASS, DSS	iso	10.76
UGC2238	cp::	H:	S2	cp:	L:	0.6(0.5)	...	2MASS, DSS	...	11.24
IR02438+2122	S2::	H:	S2	S2:	L	0.8(0.8)	...	2MASS, DSS	...	11.08
UGC2369	cp	H	H	cp	H	0.2(0.3)	11.5	2MASS	a	11.58
NGC1143/4	S2	S2	S2	S2	S2	1(1)	13.3	2MASS	a	11.39
UGC2403	cp	H	H	cp	H	0.2(0.3)	-2	2MASS, DSS	iso	10.86
NGC1204	cp	H	H	cp	L:	0.3(0.4)	-2	2MASS, DSS	iso	10.81
NGC1266	L:	L	L	L	L	0.8(1)	-2	2MASS, DSS	iso	10.34
NGC1377	10.04
IR03359+1523	H	H	H	H	H	0(0.2)	6.9	2MASS	b	11.47
UGC2982	H	H	H	H	H	0(0.1)	-2	2MASS, DSS	iso	11.15
ESO550-IG025:S	cp	H	H	cp	L:	0.3(0.4)	4.5	2MASS	b	11.44
ESO550-IG025:N	cp	H	L	cp:	L	0.4(0.4)	4.5	2MASS	b	...
NGC1614	cp	H	H	cp	H:	0.2(0.4)	-1	2MASS, DSS	cde	11.58
ESO484-G036	10.80
ESO485-G003	H	H	H	H	H	0(0.1)	-2	2MASS, DSS	iso	10.82
IC398	10.82
NGC1797	H	H	H	H	H	0(0.2)	-2	2MASS, DSS	iso	10.97
IR05187-1017	L::	L	L	L	L	0.6(0.7)	-2	2MASS, DSS	iso	11.23
*IR05189-2524	S2::	S2	S2	S2	S2	1(1)	-2	2MASS, DSS	iso	12.09
NGC2388	H	H	H	H	H	0(0.2)	59.5	DSS	a	11.18
IR08339+6517	H	H	H	H	H	0(0.2)	-2	2MASS, DSS	iso	11.08
NGC2623	11.55
*IR08572+3915	cp	L	S2	cp::	L:	0.5(0.4)	59.1	2MASS	a	12.11
NGC2785	cp	H	H	cp	H:	0.3(0.3)	86.5	DSS	a	10.70
UGC4881:SW	cp	H	H	cp	H:	0.3(0.3)	8.3	2MASS	b	11.70
UGC4881:NE	cp::	H	H	cp	H:	0.2(0.3)	8.3	2MASS	b	...
UGC5101	S2	H	S2	S2:	L	0.6(0.8)	-1	2MASS, DSS	cde	12.00
MCG+08-18-012	cp	H	H	cp	H:	0.3(0.3)	30.4	2MASS	a	11.31
NGC3110	H	H	H:	H	H	0(0.1)	100:	2MASS, DSS	a iso	11.22
IR10565+2448:W	cp	H	H	cp	H	0.2(0.2)	20.1	2MASS, DSS	a	12.00
IR10565+2448:NE
NGC3508:W	H	H	H	H	H	0(0.1)	...	2MASS, DSS	...	10.79
NGC3508:E	H	H	H:	H	H	0(0)	...	2MASS, DSS
NGC3597	H	H	H:	H	H	0(0.2)	-1	2MASS, DSS	cde	10.91
MCG+00-29-023	cp	H	H	cp	H:	0.4(0.5)	-2	2MASS, DSS	iso	11.23
UGC6436:NW	H	H	H	H	H	0(0.2)	44.4	2MASS, DSS	a	11.52
UGC6436:SE
IR12224-0624	S2::	H	...	S2::	L:	1(0.6)	-1	2MASS, DSS	cde	11.18
NGC4666	S2	S2	H:	S2:	L	0.4(0.7)	-2	2MASS, DSS	iso	11.08
IC3908	H	H	H:	H	H	0(0.1)	-2	2MASS, DSS	iso	9.45
*UGC8058	S1	S1	1(1)	-2	2MASS, DSS	iso	12.53
NGC4922	S2	S2	S2	S2	L	0.6(0.6)	9.4	2MASS	b	11.25
MCG-02-33-098:W	H	H	H	H	H:	0(0.1)	3.3	2MASS	b	11.05
MCG-02-33-098:E	H	H	H:	H	H	0(0)	3.3	2MASS	b	...
IC860	11.12
UGC8335:NW	cp	H	H	cp	H:	0.4(0.4)	19	2MASS	a	11.76
UGC8335:SE	cp	H	H	cp	H	0.3(0.3)	19	2MASS	a	...
UGC8387	cp	H	L	cp:	L	0.5(0.4)	26.5	2MASS	a	11.58
NGC5104	cp::	H	L	cp:	L	0.5(0.5)	26.5	2MASS	a	11.11
NGC5218	cp	H	L	cp	L	0.4(0.5)	46.1	2MASS	a	10.69

TABLE 2 — *Continued*

Name (1)	Spectral Type					D_{AGN} (7)	n_s kpc (8)	"reference" (9)	Morphology Class (10)	$\log(L_{\text{IR}}/L_{\odot})$ (11)
	[NII] (2)	[SII] (3)	[OII] (4)	Adopt (5)	"VO87" (6)					
NGC5256:SW	cp	H	L	cp	L	0.6(0.5)	...	2MASS, DSS	...	11.48
NGC5256:NE	S2	S2	S2	S2	S2	0.7(0.7)	...	2MASS, DSS
NGC5257/8:W	H	H	H	H	H	0(0.2)	100:	2MASS, DSS	a(iso?)	11.51
NGC5257/8:E
*UGC8696	S2	S2	S2	S2	L	0.7(0.7)	-1	2MASS, DSS	cde	12.14
NGC5430	H	H	H	H	H	0(0.2)	-2	2MASS, DSS	iso	10.88
Zw247.020	cp	H	H	cp	H:	0.1(0.4)	-2	2MASS, DSS	iso	11.32
NGC5653:W	H	H	H	H	H	0(0.1)	...	2MASS, DSS	...	11.01
NGC5653:E	H::	H	H:	H	H	0(0)	...	2MASS, DSS
NGC5676	H	H	...	H:	H	0(0.2)	-2	2MASS, DSS	iso	10.77
*IR14348-1447:SW	cp	H	S2	cp:	L:	0.6(0.4)	-1	2MASS, DSS	cde	12.26
*IR14348-1447:NE	cp	H	L	cp:	L:	0.6(0.4)	-1	2MASS, DSS	cde	...
NGC5734	11.01
UGC9618	cp	H	L	cp:	L:	0.5(0.5)	25.1	2MASS	a	11.65
Zw049.057	H::	H	H:	H	H	0(0)	-2(cl)	2MASS, DSS	iso	11.15
I Zw107:S	cp	H	S2	cp:	L	0.5(0.5)	5.4	2MASS	b	11.85
I Zw107:N	cp	H	H	cp	H	0.3(0.4)	5.4	2MASS	b	...
IR15250+3609	cp	H	S2	cp:	L:	0.4(0.4)	-1	2MASS, DSS	cde	11.97
NGC5936	cp	H	H	cp	H	0.1(0.3)	-2	2MASS, DSS	iso	11.02
NGC5953	S2	H	S2	S2:	L	0.5(0.6)	5.5	2MASS	b	10.62
*UGC9913:S	12.18
*UGC9913:N	S2::	S2	S2	S2	S2	1(1)	cde	...
IR15335-0513	S2::	H	S2	S2:	L	0.6(0.6)	-2	2MASS, DSS	iso	11.25
NGC6090:SW	H	H	H	H	H	0(0.2)	3.6	2MASS	b	11.49
NGC6090:NE	H	H	H	H	H	0(0.1)	3.6	2MASS	b	...
IR16164-0746	S2	H	S2	S2:	L	0.7(0.6)	-1	2MASS, DSS	cde	11.43
MCG+01-42-088	H	H	H	H	H	0(0.2)	11.34
NGC6181	H::	H	...	H:	H	... (0.1)	-2(cl)	2MASS, DSS	iso	10.69
NGC6240	L	L	L	L	L	0.8(0.7)	0.74	tec00	b	11.83
NGC6285/6:NW	cp	H	H	cp	H:	0.3(0.2)	31.3	2MASS	a	11.33
NGC6285/6:SE	cp	H	L	cp:	L	0.5(0.5)	31.3	2MASS	a	...
IR17132+5313:W	11.88
IR17132+5313:E	H	H	H	H	H	0(0.2)	6	2MASS	b	...
IR17138-1017	11.39
*IR17208-0014	H	H	H	H	H	0(0.2)	-1	2MASS, DSS	cde	12.40
NGC6621 ^a	H	H	H	H	H	0(0.3)	15.7	2MASS	a	11.26
IR18293-3413	H	H	H	H	H	0(0.2)	100:	2MASS, DSS	iso	11.26
NGC6670:W	H	H	H	H	H	0(0)	m	2MASS, DSS	m	11.60
NGC6670:E	H::	H	H	H	H	0(0.2)	m	2MASS, DSS	m	...
NGC6701	cp	H	H	cp	H:	0.4(0.4)	-2	2MASS, DSS	iso	11.09
ESO593-IG008:S	S2	H::	S2	S2:	L	0.4(1)	...	2MASS, DSS	...	11.86
ESO593-IG008:N	cp	H	H	cp	H	0.2(0.3)	...	2MASS, DSS
*IR19297-0406	cp	H	H	cp	H	0.4(0.3)	m	2MASS, DSS	m	12.36
NGC6926	S2::	S2	L	S2:	S2	1(0.9)	-2	2MASS, DSS	iso	11.27
Zw448.020:NW	11.89
Zw448.020:SE	H	H	H	H	H	0(0.2)	6.7	2MASS	b	...
ESO286-IG019	H	H	H	H	H:	0(0.2)	-1	2MASS	cde	11.98
ESO343-IG013:S	cp	H	H	cp	H:	0.2(0.3)	3.9	2MASS	b	11.05
ESO343-IG013:N	cp	H	H	cp	H	0.2(0.2)	3.9	2MASS	b	...
NGC7130	S2	S2	L	S2:	L	0.9(0.7)	-2	2MASS, DSS	iso	11.31
IC5179	H::	H	H	H	H	0(0)	-2	2MASS, DSS	iso	11.12
ESO602-G025	cp	H	H	cp:	L:	0.4(0.4)	-2	2MASS, DSS	iso	11.25
ESO534-G009	L::	L	L	L	L	0.8(0.9)	-2	2MASS, DSS	iso	10.61
UGC12150	cp	H	H	cp	H:	0.1(0.3)	-2	2MASS, DSS	iso	11.29
*IR22491-1808	H	H	H	H	H	0(0.2)	3.9	2MASS	b	12.08
NGC7469	S1	S1	1(1)	19	2MASS	a	11.60
Zw453.062	S2	H	S2	S2:	L	0.6(0.7)	-2	2MASS, DSS	iso	11.28
Zw475.056	S2	S2	S2	S2	S2	0.7(0.8)	-2	2MASS, DSS	iso	11.53
NGC7591	S2	H	S2	S2:	L	0.5(0.6)	-2	2MASS, DSS	iso	11.04
NGC7592:W	S2	S2	S2	S2	S2	0.7(0.7)	23.7	2MASS	a	11.33
NGC7592:E	H	H	H	H	H	0(0.1)	23.7	2MASS	a	...
NGC7674	S2	S2	S2	S2	S2	1(1)	17.4	2MASS	a	11.49
NGC7679	S2	S2	S2	S2	S2	0.7(0.7)	-2	2MASS, DSS	iso	11.05
NGC7714	cp	H	H	cp	H	0.4(0.3)	15.5	2MASS	a	10.67
*IR23365+3604	cp	H	H	cp	L	0.3(0.4)	-2	2MASS, DSS	iso	12.14
NGC7771	cp	H	H:	cp	H	0.3(0.3)	16.8	2MASS	a	11.35
NGC7771:S	H	H	H	H	H	0(0.2)	16.8	2MASS	a	...
MCG+03-60-036	H	H	H	H	H	0(0.3)	100:	2MASS, DSS	iso	11.41

TABLE 2 — *Continued*

Name (1)	Spectral Type					D_{AGN} (7)	ns kpc (8)	“reference” (9)	Morphology Class (10)	$\log(L_{\text{IR}}/L_{\odot})$ (11)
	[NII] (2)	[SII] (3)	[OI] (4)	Adopt (5)	“VO87” (6)					

NOTE. — Col. (1): Galaxy Name. * denotes ULIRGs. Col. (2) to Col. (4): Optical spectral types derived in this work from the [N II] $\lambda 6583$, [S II] $\lambda \lambda 6716, 6731$, and [O I] $\lambda 6300$ diagrams respectively. The typical uncertainty on the emission-line ratios is $\sim 10\%$; colons in Col. (3) and Col. (4) indicate larger uncertainty of the line ratios of $\sim 25\%$ for [S II]/ $H\alpha$ and [O I]/ $H\alpha$, respectively; double colons in Col. (2) indicate larger uncertainty of the line ratios of $\sim 25\%$ for [O III]/ $H\beta$. Col. (5) is the adopted spectral type using the 2-of-3 scheme; colons indicate the object does not have the same spectral type in all 3 diagrams, i.e., the ambiguous class. Double colons means the classification does not agree on any of the diagrams, the classification in those rare cases is highly uncertain. For comparison, Col. (6) lists the VO87 classification results (Veilleux et al. 1999). Symbols: H = star-forming galaxies, L = LINERs, S2 = Seyfert 2 galaxies, S1 = Seyfert 1 galaxies, cp = starburst-AGN composite galaxies. Col. (7): D_{AGN} defined on the [O I]/ $H\alpha$ diagram, for comparison, in the bracket we also list the D_{AGN} derived from the [N II]/ $H\alpha$ diagram (see Appendix A). Col. (8), projected nuclear separation in kpc. -1: single nucleus with tidal features; -2: isolated systems “:”: lower limit; “m”: multiple (more than two) interacting objects; “cl”: member of clusters. Col. (9): references used to obtain projected separation or tidal features. 2MASS: 2MASS images (K_s -band); DSS: DSS images; tec00: Tecza et al. (2000). Col. (10): adopted morphology class, a: wide binary; b: close binary; cde: single merger (either diffuse merger, compact merger, or old merger); iso: isolated system; m: multiple mergers. Col. (11): $\log(L_{\text{IR}}/L_{\odot})$, data from Kim et al. (1995b).

^a Line flux of this object given in Kim et al. (1995b) Table 1A has a sign error

TABLE 3
SPECTRAL CLASSIFICATION RESULT AND MORPHOLOGY FOR THE SW01 SAMPLE

Name (1)	Spectral Type				D_{AGN} (6)	ns kpc (7)	“reference” (8)	Morphology Class (9)	$\log(L_{\text{IR}}/L_{\odot})$ (10)
	[NII] (2)	[SII] (3)	[OI] (4)	Adopt (5)					
*IRAS00091–0738	-1	2MASS	cde	12.16
IRAS00163–1039(Arp256) obj1	H	H	H	H	0(0.2)	27.6	2MASS	a	11.40
IRAS00163–1039(Arp256) obj2	H	H	H	H	0(0.2)	27.6	2MASS	a	11.40
IRAS00198–7926	S2	S2	S2	S2	0.6(0.6)	17.5	2MASS	a	11.98
IRAS00247–0203(NGC118)	-2	2MASS	iso	11.35
IRAS00317–2804(NGC150)	cp	H	H	cp	0.4(0.4)	-2	2MASS	iso	10.14
IRAS00335–2732	cp	H	S2	cp:	0.5(0.4)	6.6	cb96	b	11.93
IRAS00344–3349 obj1	H	H	H	H	0(0.3)	1.4	hv94	b	11.18
IRAS00344–3349 obj2	H	H	H	H	0(0.3)	1.4	hv94	b	11.18
IRAS00366+0035(NGC192)	cp	H	H	cp	0.3(0.4)	33.6	2MASS	a	10.55
IRAS00450–2533(NGC253)	cp	H	H	cp	0.2(0.4)	60:	DSS	a	10.41
IRAS00510–0901(NGC0291)	S2	S2	S2	S2	0.9(0.9)	-2	2MASS	iso	10.77
IRAS00535–5044	H	H	H	H	0(0)	26.1	2MASS	a	10.62
IRAS01025–6423	cp	H	H	cp	0.6(0.3)	-1	2MASS	cde	10.75
IRAS01050–3305	29.	2MASS	a	11.31
IRAS01077–1707	41.5	2MASS	a	11.56
IRAS01103–4158	cp	H	H	cp	0.3(0.4)	-2	2MASS	iso	11.13
IRAS01159–4443 obj1	cp	H	H	cp	0.1(0.3)	7.3	2MASS	b	11.31
IRAS01159–4443 obj2	cp	L	S2	cp::	0.1(0.3)	7.3	2MASS	b	11.31
IRAS01165–1719	48.5	2MASS	a	10.92
IRAS01167+0418(NGC0567)	-2	2MASS	iso	11.26
IRAS01171+0308(NGC470)	H	H	H	H	0(0.1)	-2	2MASS	iso	10.39
IRAS01249–0848(MRK0995)	-1	2MASS	cde	11.66
IRAS01268–3551(NGC0574)	m	2MASS	m	10.80
IRAS01329–4141(NGC625)	-2	2MASS	iso	8.48
IRAS01341–3734(NGC633)	cp	H	H	cp	0.2(0.3)	21.9	2MASS	a	10.94
IRAS01346+0537(NGC632)	18.2	DSS	a	10.45
IRAS01348–8526	-2	2MASS	iso	10.42
*IRAS01388–4618	-1	2MASS	cde	12.03
IRAS01544–0538(NGC762)	H	H	H	H	0(0.2)	-2	2MASS	iso	10.68
IRAS02015–2333(NGC808)	H	H	H	H	0(0.2)	-2	2MASS	iso	10.77
IRAS02062+0744(NGC827)	-2	2MASS	iso	10.52
IRAS02082–1600(NGC814)	15.1	DSS	a	9.75
IRAS02092–0932(NGC853)	-2	2MASS	iso	9.58
IRAS02111+0352	-2	2MASS	iso	10.26
IRAS02160–0650	cp	H	H	cp	0.4(0.4)	41.9	2MASS	a	11.48
IRAS02242–1444	H	H	H	H	0(0.1)	8.5	vva68	b	10.3
IRAS02303–2954	H	H	H	H	0(0.1)	100:	DSS	iso	10.6
IRAS02304+0012	S2	S2	S2	S2	0.8(0.9)	-2	2MASS	iso	10.88
IRAS02360–0653(NGC1022)	H	H	H	H	0(0.2)	100:	2MASS	iso	10.38
IRAS02401–0013(NGC1068)	S2	S2	S2	S2	1(1)	-2	2MASS	iso	11.38
IRAS02493–1651	10.5	2MASS	a	10.3
IRAS02521–1013(NGC1140)	H	H	H	H	0(0.1)	-2	2MASS	iso	9.58
IRAS02530+0211	cp	H	H	cp	0.3(0.4)	-2	2MASS	iso	10.99
IRAS02557–1033	26.2	2MASS	a	10.51
IRAS02572+0234	9.2	2MASS	b	10.23
IRAS03022–1232(NGC1204)	-2	2MASS	iso	10.85
IRAS03064–0308(NGC1222)	H	H	H	H	0(0.2)	-2	2MASS	iso	10.68
IRAS03144+0104	6.6	2MASS	b	10.85
IRAS03229–0618	S1	1(1)	52.8	DSS	a	11.17
IRAS03344–2103(NGC1377)	-2	2MASS	iso	9.88
IRAS03348–3609(NGC1386)	H	H	H	H	0(0.1)	100:	DSS	iso	9.35
IRAS03348–0508	S2	S2	S2	S2	1(1)	-2	2MASS	iso	10.64

TABLE 3 — *Continued*

Name (1)	Spectral Type				D_{AGN} (6)	n_s kpc (7)	“reference” (8)	Morphology Class (9)	$\log(L_{\text{IR}}/L_{\odot})$ (10)
	[NII] (2)	[SII] (3)	[OI] (4)	Adopt (5)					
IRAS03372–1841(NGC1042)	cp	H	H	cp	0.2(0.4)	-2	2MASS	iso	10.39
IRAS03443–1642	-2	2MASS	iso	9.55
IRAS03467–2216	cp	H	H	cp	0.3(0.2)	-2	2MASS	iso	10.55
IRAS03524–2038(NGC1482)	100:	2MASS	iso	10.61
IRAS03536–1351	-1	2MASS	cde	11.05
*IRAS03575–6132	S2	S2	S2	S2	0.9(1)	-1	2MASS	cde	12.21
IRAS03594–6746(NGC1511)	H	H	H	H	0(0.1)	100:m	2MASS	iso	10.19
IRAS04001–1811	S2	S2	S2	S2	0.6(0.6)	-2	2MASS	iso	11.01
IRAS04118–3207	S2	H	H	H:	0.4(0.5)	-2	2MASS	iso	10.95
IRAS04131–2836(NGC1540) obj1	H	H	H	H	0(0.1)	8.7	2MASS	b	10.68
IRAS04131–2836(NGC1540) obj2	H	H	H	H	0(0.1)	8.7	2MASS	b	10.68
IRAS04133+0803	-2	2MASS	iso	11.49
IRAS04257–4913	cp	H	H	cp	0.1(0.2)	46.	2MASS	b	11.75
IRAS04259–0440	S2	H	S2	S2:	0.7(0.6)	-2	2MASS	iso	10.69
IRAS04273–3735	cp	H	H	cp	0.2(0.3)	-2	2MASS	iso	10.98
IRAS04315–0840(NGC1614)	cp	H	H	cp	0.3(0.4)	0.3	2MASS	b	11.57
IRAS04332+0209	-2	2MASS	iso	10.46
IRAS04339–1028	S1	1(1)	36	2MASS	a	11.32
IRAS04385–0828	-2	2MASS	iso	10.67
IRAS04449–5920(NGC1672)	-2	2MASS	iso	10.39
IRAS04501–3304	cp	H	H	cp	0.3(0.3)	-2	2MASS	iso	11.07
IRAS04502+0258	13.8	2MASS	a	10.48
IRAS04520+0311(NGC1691)	cp	H	H	cp	0.1(0.3)	-2	2MASS	iso	10.88
IRAS04591–0419	-2	2MASS	iso	10.5
IRAS05053–0805(NGC1797)	H	H	H	H	0(0.2)	-2	2MASS	iso	10.94
IRAS05059–3734(NGC1808)	H	H	H	H	0(0.2)	-2	2MASS	iso	10.47
IRAS05066+0844	-1	2MASS	cde	11.33
IRAS05095–1511	2.6	vva68	b	10.24
IRAS05100+0614	72.	2MASS	a	11.40
IRAS05144–1224	-2	2MASS	iso	9.65
IRAS05170+0535	-2	2MASS	iso	11.78
*IRAS05189–2524	-1	2MASS	cde	12.07
IRAS05238–4602	S2	S2	S2	S2	0.8(0.9)	-1	2MASS	cde	11.46
IRAS05246+0103	9.	2MASS	b	12.07
IRAS05409–2405 obj1	H	H	H	H	0(0.1)	15.	2MASS	a	11.00
IRAS05409–2405 obj2	2MASS	a	11.00
IRAS05471–4746	S2	S2	S2	S2	0.6(0.6)	-1	2MASS	cde	11.60
IRAS05486–2259	cp	H	H	cp	0.3(0.4)	1.6	2MASS	b	11.05
IRAS05497–0728(NGC2110)	L	L	L	L	1(0.9)	-2	2MASS	iso	10.08
IRAS05535–1902	-2	2MASS	iso	10.12
IRAS05562–6933(NGC2150)	H	H	H	H	0(0.2)	-2	2MASS	iso	10.77
IRAS06111–7020	H	H	H	H	0(0)	-2	2MASS	iso	10.99
IRAS06259–4708 obj1	H	H	H	H	0(0.2)	10.3	2MASS	a	11.10
IRAS06259–4708 obj2	cp	H	H	cp	0.1(0.3)	10.3	2MASS	a	...
IRAS06592–6313	cp	H	H	cp	0.1(0.4)	-2	2MASS	iso	11.10
IRAS06593–7551	H	H	H	H	0(0.1)	-2	2MASS	iso	10.07
IRAS07027–6011	S2	S2	S2	S2	0.9(0.8)	50.	2MASS	a	11.41
IRAS07269–6811	8.6	2MASS	b	11.66
IRAS08007–6600	cp	0.4(0.3)	-2	2MASS	iso	11.52
IRAS08087+0347(NGC2358)	cp	0.2(0.3)	-2	2MASS	iso	10.47
IRAS08169+0448(NGC2561)	100:	DSS	iso	10.37
IRAS08225–6936	H	H	H	H	0(0.1)	-2	2MASS	iso	10.52
IRAS08438–1510	cp	H	S2	cp:	0.5(0.5)	-2	2MASS	iso	10.75
IRAS08480–0254(MRK1414)	H	H	H	H	0(0.1)	-2	2MASS	iso	10.46
IRAS08511–1028	H	H	H	H	0(0.2)	-2	2MASS	iso	10.88
IRAS08561+0629(NGC2718)	H	H	H	H	0(0.2)	-2	2MASS	iso	10.48
IRAS08594+0829	-2	2MASS	iso	10.0
IRAS09004–2031	H	H	H	H	0(0.2)	7.	2MASS	b	10.39
IRAS09070+0722	H	H	H	H	0(0.2)	-2	2MASS	iso	10.66
IRAS09143+0939	-2	2MASS	iso	11.5
IRAS09248–1918	cp	H	H	cp	0.2(0.3)	-2	2MASS	iso	10.70
IRAS09324–2142	S2	S2	S2	S2	0.8(0.8)	16.3	2MASS	a	10.47
IRAS09395+0454(NGC2966)	H	H	H	H	0(0.2)	100:	DSS	iso	10.37
IRAS09426–1928	cp	H	H	cp	0.4(0.3)	29.	2MASS	a	10.52
IRAS09433–1531	H	H	H	H	0(0.1)	5.	2MASS	b	10.75
IRAS09432–1405(NGC2993)	H	H	H	H	0(0.2)	25.	2MASS	a	10.43
IRAS09521+0930(NGC3049)	H	H	H	H	0(0.1)	-2	2MASS	iso	9.44
IRAS09591–1317	-2	2MASS	iso	10.57
IRAS10036–0057	cp	H	H	cp	0.6(0.4)	3.5	2MASS	b	11.34
IRAS10042–2941(NGC3125) obj1	H	H	H	H	0(0.2)	0.6	2MASS	b	9.22
IRAS10042–2941(NGC3125) obj2	H	H	H	H	0(0.2)	0.6	2MASS	b	9.22
IRAS10057–3343	cp	H	H	cp	0.3(0.5)	-2	2MASS	iso	11.13
IRAS10140–3318(IC2560)	S2	S2	S2	S2	1(1)	-2	2MASS	iso	10.20
IRAS10219–2828	7.6	2MASS	b	11.17

TABLE 3 — *Continued*

Name (1)	Spectral Type				D_{AGN} (6)	n_s kpc (7)	“reference” (8)	Morphology Class (9)	$\log(L_{\text{IR}}/L_{\odot})$ (10)
	[NII] (2)	[SII] (3)	[OI] (4)	Adopt (5)					
IRAS10221–2317	S2	H	S2	S2:	0.5(0.5)	-2	2MASS	iso	10.80
IRAS10295–1831	S2	H	S2	S2:	0.6(0.6)	-2	2MASS	iso	11.30
IRAS10295–3435(NGC3281)	S2	S2	S2	S2	1(1)	-2	2MASS	iso	10.69
IRAS10323–2819	H	H	H	H	0(0.3)	6.8	2MASS	b	10.23
IRAS11083–2813	S1	1(1)	-2	2MASS	iso	11.00
*IRAS11095–0238	-1	2MASS	cde	12.17
IRAS11100+0919(IC676)	H	H	H	H	0(0.2)	-2	2MASS	iso	9.50
IRAS11122–2327(NGC3597)	H	H	H	H	0(0.2)	-1	2MASS	cde	10.81
IRAS11149+0449(NGC3611)	H	H	H	H	0(0.2)	100:	DSS	iso	9.77
IRAS11178+0351(NGC3633)	-2	2MASS	iso	10.06
IRAS11186–0242	-2	2MASS	iso	11.22
IRAS11264+0923	-2	2MASS	iso	10.90
IRAS11273–0607	-2	2MASS	iso	11.53
IRAS11316–0934(NGC3732)	H	H	H	H	0(0.2)	-2	2MASS	iso	9.82
IRAS11365–3727(NGC3783)	S1	1(1)	-2	2MASS	iso	10.29
IRAS11396+0036	H	H	H	H	0(0.2)	-1	2MASS	cde	10.75
IRAS11409–1631	H	H	H	H	0(0)	1.2	2MASS	b	10.44
IRAS11430+0330(NGC3849)	-2	2MASS	iso	10.80
IRAS11442–2738(NGC3885)	-2	2MASS	iso	10.22
IRAS11514–2253(NGC3955)	-2	2MASS	iso	9.77
IRAS12056+0309(NGC4123)	H	H	H	H	0(0.2)	-2	2MASS	iso	9.73
IRAS12063–3625	-2	2MASS	iso	10.39
IRAS12071–0444	-1	2MASS	cde	12.29
IRAS12121–3513	H	H	H	H	0(0.2)	61	DSS	a	10.57
IRAS12174–1706	H	H	H	H	0(0.1)	-2	2MASS	iso	8.89
IRAS12193–4303	4.	2MASS	b	11.10
IRAS12195–3312(NGC4304)	H	H	H	H	0(0.2)	-2	2MASS	iso	10.32
IRAS12231+0050(NGC4385)	cp	H	H	cp	0.3(0.3)	-2	2MASS	iso	10.04
IRAS12240+0414 (NGC4412)	S2	S2	S2	S2	0.5(0.6)	-2	2MASS	iso	9.70
IRAS12243–0036 (NGC4418)	-2	2MASS	iso	10.86
IRAS12246+0941(NGC4424)	-2	2MASS	iso	8.33
IRAS12286–2600	cp	H	H	cp	0.1(0.2)	-2	2MASS	iso	10.86
IRAS12329–3938(NGC4507)	S2	S2	S2	S2	1(0.9)	-2	2MASS	iso	10.51
IRAS12370–0504(NGC4593)	S1	1(1)	-2	2MASS	iso	10.11
IRAS12381–3628 (IC3639)	S2	S2	S2	S2	1(1)	-2	2MASS	iso	10.67
IRAS12398–0641 (NGC4628)	-2	2MASS	iso	10.21
IRAS12456–0303(NGC4691)	H	H	H	H	0(0.1)	-2	2MASS	iso	9.90
IRAS12465–1108 (NGC4700)	H	H	H	H	0(0)	-2	2MASS	iso	9.43
IRAS12476+0751	-1	2MASS	cde	11.37
IRAS12499–0930(MRK1337)	H	H	H	H	0(0.2)	39	DSS	a	10.11
IRAS12504–2711	-2	2MASS	iso	10.49
IRAS12540–4251	cp	H	S2	cp:	0.5(0.5)	-2	2MASS	iso	10.41
IRAS12542–0815(NGC4818)	cp	H	H	cp	0.5(0.3)	-2	2MASS	iso	10.04
IRAS12550–2929	cp	H	H	cp	0.2(0.3)	-2	2MASS	iso	10.43
IRAS12596–1529 obj2	cp	H	H	cp	0.1(0.3)	-2	2MASS	b	10.93
IRAS12596–1529 obj3	H	H	H	H	0(0.1)	1.2	ke01	b	...
IRAS13035–4008	S1	1(1)	-2	2MASS	iso	10.85
IRAS13062–1514 (NGC4984)	cp	H	H	cp	0.2(0.4)	-2	2MASS	iso	9.87
IRAS13067–0500(NGC4990)	cp	H	H	cp	0.4(0.3)	-2	2MASS	iso	10.15
IRAS13081–4557	H	H	H	H	0(0.2)	-2	2MASS	iso	10.10
IRAS13123–1541(NGC5038)	cp	H	H	cp	0.2(0.5)	100:	DSS	iso	10.29
IRAS13154–0002	H	H	H	H	0(0.2)	36.8	DSS	a	11.18
IRAS13157+0635	16.2	2MASS	a	10.87
IRAS13167–1435(NGC5073)	H	H	H	H	0(0.2)	-2	2MASS	iso	10.50
IRAS13183–1212(NGC5097)	H	H	H	H	0(0.1)	-2	2MASS	iso	9.91
IRAS13197–1627	H	H	H	H	0(0.2)	32.	2MASS	a	11.07
IRAS13197–3928	H	H	H	H	0(0.2)	-1	2MASS	cde	11.09
IRAS13229–2934(NGC5135)	S2	S2	S2	S2	0.8(0.8)	-2	2MASS	iso	11.16
IRAS13244–4240	H	H	H	H	0(0.2)	-1	2MASS	cde	11.17
IRAS13286–3432(NGC5188)	cp	H	H	cp	0.1(0.3)	-2	2MASS	iso	10.72
IRAS13303–1559	H	H	H	H	0(0.2)	-2	2MASS	iso	11.00
IRAS13333–1700	-1	2MASS	cde	11.58
IRAS13336–0046 obj1	cp	H	H	cp	0.2(0.4)	12.2	2MASS	a	11.67
IRAS13336–0046 obj2	12.2	2MASS	a	11.67
IRAS13370–3123	-2	2MASS	iso	9.05
IRAS13373+0105(NGC5257)	32.7	2MASS	a	11.43
IRAS13379+0501	cp	H	H	cp	0.1(0.3)	-2	2MASS	iso	10.87
IRAS14002–4108(NGC5408)	H	H	H	H	0(0.2)	-2	2MASS	iso	8.37
IRAS14036+0234	18.6	2MASS	a	11.12
IRAS14104–1350	S2	S2	S2	S2	0.5(0.6)	-1	2MASS	cde	11.86
IRAS14106–0258(NGC5506)	S2	S2	S2	S2	1(0.9)	26.2	DSS	a	10.28
IRAS14137–4444(IC4390)	-2	2MASS	iso	9.75
IRAS14150–0711(NGC5534)	H	H	H	H	0(0.2)	4.5	2MASS	b	10.22
IRAS14209–1306	-1	2MASS	cde	10.78

TABLE 3 — *Continued*

Name (1)	Spectral Type				D_{AGN} (6)	n_s kpc (7)	"reference" (8)	Morphology Class (9)	$\log(L_{\text{IR}}/L_{\odot})$ (10)
	[NII] (2)	[SII] (3)	[OI] (4)	Adopt (5)					
IRAS14216–1632(NGC5597)	100:	DSS	iso	10.54
IRAS14294–4357(NGC5643)	S2	S2	S2	S2	1(1)	-2	2MASS	iso	10.10
IRAS14299+0817(NGC5665)	H	H	H	H	0(0.1)	-2	2MASS	iso	10.29
IRAS14309–1424	S2	S2	S2	S2	0.7(0.7)	6.7	2MASS	b	10.5
IRAS14353–0011 (NGC5691)	H	H	H	H	0(0.1)	-2	2MASS	iso	9.85
IRAS14376–0004(NGC5713)	cp	H	H	cp	0.1(0.2)	-2	2MASS	iso	10.61
IRAS14384–3742	-2	2MASS	iso	11.36
IRAS14430–3728	-2	2MASS	iso	10.77
IRAS14483+0519(NGC5765)	S2	S2	S2	S2	0.8(0.8)	11.5	2MASS	a	11.19
IRAS14515–1504	-2	2MASS	iso	11.01
IRAS14575–2615 obj1	H	S2	S2	S2:	... (0.3)	10.4	DSS	a	10.65
IRAS14575–2615 obj2	H	H	H	H	0(0.3)	10.4	DSS	a	10.65
IRAS15028+0820	-1	2MASS	cde	11.41
IRAS15065–1107(NGC5861)	100:	DSS	iso	10.29
IRAS15150–1724(NGC5890)	-2	2MASS	iso	9.82
IRAS15172–3115	H	H	H	H	0(0.2)	-1	2MASS	cde	10.81
IRAS15188–0711	30.	2MASS	a	9.87
IRAS15229+0511	84.5	DSS	a	11.18
IRAS15257+0302	H	H	H	H	0(0.1)	-2	2MASS	iso	11.25
IRAS15268–7757	H	H	H	H	0(0.2)	-2	2MASS	iso	9.86
IRAS15320–2601	-1	2MASS	cde	11.97
IRAS15361–0313	-2	2MASS	iso	10.99
IRAS15437+0234(NGC5990) obj1	S2	S2	S2	S2	0.6(0.7)	33.3	2MASS	a	10.53
IRAS15437+0234(NGC5990) obj2	S2	S2	S2	S2	0.6(0.7)	33.3	2MASS	a	10.53
IRAS15456–1336(NGC5995)	S1	1(1)	-2	2MASS	iso	11.47
*IRAS15462–0450	-1	2MASS	cde	12.37
IRAS16235+0301	-2	2MASS	iso	9.58
IRAS16399–0937 obj1	cp	H	H	cp	0.2(0.2)	3.5	DSS	b	11.07
IRAS16399–0937 obj2	L	L	L	L	0.7(0.7)	3.5	DSS	b	...
IRAS16487–0222	-2	2MASS	iso	11.35
IRAS16504+0228(NGC6240)	L	L	L	L	0.8(0.7)	0.74	tec00	b	11.83
IRAS17138–1017	cp	H	H	cp	0.2(0.3)	-1	2MASS	cde	11.50
*IRAS17324–6855	H	H	H	H	0(0.2)	3.6	2MASS	b	12.15
IRAS17467+0807	H	H	H	H	0(0.2)	-2	2MASS	iso	10.77
IRAS18078–5815	cp	H	H	cp	0.4(0.3)	-2	2MASS	iso	10.13
IRAS18093–5744 obj1	H	H	H	H	0(0.2)	8.7	2MASS	b	10.68
IRAS18093–5744 obj2	H	H	H	H	0(0.2)	8.7	2MASS	b	10.68
IRAS18097–6006	cp	H	H	cp	0.2(0.3)	-2	2MASS	iso	10.89
IRAS18325–5926	S2	H	S2	S2:	0.8(0.7)	-2	2MASS	iso	11.10
IRAS18429–6312(IC4769)	S2	S2	S2	S2	1(1)	24.8	DSS	a	10.73
IRAS18432–6024	3.8	2MASS	b	11.48
IRAS18515–5347(NGC6708)	H	H	H	H	0(0)	-2	2MASS	iso	10.17
IRAS19184–6822	H	H	H	H	0(0.2)	-2	2MASS	iso	10.64
IRAS19254–7245	S1	1(1)	9.3	2MASS	b	11.99
IRAS19335–2011 obj1	H	H	H	H	0(0.2)	7.6	2MASS	b	11.46
IRAS19335–2011 obj2	H	H	H	H	0(0.2)	7.6	2MASS	b	11.46
IRAS19393–5846(NGC6810)	cp	H	H	cp	0.4(0.3)	-2	2MASS	iso	10.6
IRAS19412–3305	S2	S2	S2	S2	0.6(0.7)	-2	2MASS	iso	11.16
IRAS19466–3649	15.2	2MASS	a	10.62
IRAS19543–3804	S2	S2	S2	S2	1(1)	-2	2MASS	iso	11.07
IRAS19594–2021	-2	2MASS	iso	10.81
*IRAS20046–0623	cp	L	S2	cp:	0.5(0.3)	21.5	DSS	a	12.08
IRAS20082+0058	cp	H	H	cp	0.3(0.5)	57.4	DSS	a	10.97
IRAS20104–4430	H	H	H	H	0(0.2)	-2	2MASS	iso	10.81
IRAS20114–5803(IC4980)	S2	S2	S2	S2	1(1)	-2	2MASS	iso	10.52
IRAS20122–0955	-1	2MASS	cde	11.52
IRAS20178–0052	cp	H	H	cp	0.2(0.3)	48.8	DSS	a	10.77
IRAS20205–4409(IC4946)	cp	H	H	cp	0.1(0.3)	-2	2MASS	iso	10.34
IRAS20244–5151	cp	H	H	cp	0.4(0.3)	-2	2MASS	iso	10.75
IRAS20272–4738(NGC6918)	cp	H	H	cp	0.1(0.3)	-2	2MASS	iso	10.18
IRAS20273–1523	H	H	H	H	0(0.2)	-2	2MASS	iso	10.39
IRAS20332+0805	cp	H	H	cp	0.1(0.3)	-2	2MASS	iso	11.03
IRAS20481–5715(IC5063)	S2	S2	S2	S2	1(1)	-2	2MASS	iso	10.76
IRAS20551–4250	cp	H	H	cp	0.4(0.2)	-1	2MASS	cde	11.97
IRAS21023–4258	H	H	H	H	0(0.2)	-2	2MASS	iso	10.01
IRAS21052+0340 obj1	cp	H	H	cp	0.3(0.2)	34.	2MASS	a	11.06
IRAS21052+0340 obj2	cp	H	H	cp	0.3(0.2)	34.	2MASS	a	11.06
IRAS21116+0158(IC368)	S2	S2	S2	S2	0.9(1)	100:	DSS	iso	10.56
IRAS21330–3846	H	H	H	H	0(0.2)	4.	2MASS	b	11.05
IRAS21497–0824	S2	S2	S2	S2	1(1)	-2	2MASS	iso	11.26
IRAS21504–0628	cp	H	L	cp:	0.5(0.3)	-1	2MASS	cde	11.92
IRAS21522–4717	H	H	H	H	0(0.1)	-2	2MASS	iso	10.73
IRAS22007+0019(NGC7189)	S2	S2	S2	S2	0.6(0.7)	-2	2MASS	iso	11.18
IRAS22045+0959(NGC7212)	S2	S2	S2	S2	1(1)	7.	2MASS	b	11.09

TABLE 3 — *Continued*

Name (1)	Spectral Type				D_{AGN} (6)	ns kpc (7)	“reference” (8)	Morphology Class (9)	$\log(L_{\text{IR}}/L_{\odot})$ (10)
	[NII] (2)	[SII] (3)	[OI] (4)	Adopt (5)					
IRAS22072–3620(IC5169)	cp	H	H	cp	0.4(0.5)	-2	2MASS	iso	10.28
IRAS22115–3013	H	H	H	H	0(0.1)	-2	2MASS	iso	10.6
IRAS22127–4605(NGC7233)	H	H	H	H	0(0.1)	13.1	2MASS	a	10.01
IRAS22132–3705(IC5183)	-2	2MASS	iso	11.13
IRAS22225–3136	4.9	2MASS	b	11.16
IRAS22287–1917	cp	H	H	cp	0.5(0.5)	-2	2MASS	iso	11.26
IRAS22397–3726	cp	H	S2	cp:	0.5(0.5)	-2	2MASS	iso	10.99
IRAS22467–4906	S2	H	S2	S2:	0.5(0.5)	-1	2MASS	cde	11.70
IRAS23007+0836(NGC7469)	S1	1(1)	25.1	2MASS	a	11.58
IRAS23011+0046	-2	2MASS	iso	11.31
IRAS23023–4322(NGC7476)	H	H	H	H	0(0.2)	-2	2MASS	iso	10.19
IRAS23050+0359	cp	H	H	cp	0.2(0.2)	-1	2MASS	cde	11.61
IRAS23069–4341(NGC7496)	H	H	H	H	0(0.2)	-2	2MASS	iso	10.13
IRAS23128–5919	4.1	2MASS	b	11.95
IRAS23134–4251(NGC7552)	H	H	H	H	0(0.2)	-2	2MASS	iso	10.98
IRAS23156–4238(NGC7582)	H	H	H	H	0(0.1)	71.7	DSS	a	10.79
IRAS23157–0441(NGC7592) obj1	S2	S2	S2	S2	0.6(0.6)	7.	DSS	b	11.34
IRAS23157–0441(NGC7592) obj2	H	H	H	H	0(0.1)	7.	DSS	b	...
IRAS23192–4245(NGC7632)	-2	2MASS	iso	11.43
IRAS23201+0805	S2	S2	S2	S2	0.8(0.8)	-2	2MASS	iso	11.33
IRAS23204+0601	-1	2MASS	cde	11.80
IRAS23215–1208	-2	2MASS	iso	10.96
IRAS23254+0830(NGC7674)	S2	S2	S2	S2	1(1)	17.4	2MASS	a	11.52
IRAS23262+0314(NGC7679)	S1	1(1)	-2	2MASS	iso	11.07
IRAS23336+0152(NGC7714)	H	H	H	H	0(0.3)	20.5	2MASS	a	10.72
IRAS23414+0014(NGC7738)	cp	H	H	cp	0.3(0.5)	-2	2MASS	iso	11.08

NOTE. — We only list the spectral type results for galaxies having available line ratios with $S/N > 3\sigma$ in all three BPT diagrams. The projected radius used for searching companions is ~ 100 kpc. Col. (1) to Col. (6), the same as Table 2. Col. (7), projected nuclear separation. -1: single nucleus with tidal features; -2: isolated systems “:”: lower limit; “m”: multiple (more than two) interacting objects. Col. (8), references used to obtain projected separation. 2MASS: 2MASS images (K_s -band); DSS: DSS images; cb96: Clements & Baker (1996); hv95: Heisler & Vader (1995); vva68: Vorontsov-Velyaminov & Arhipova (1968); ke01: Kewley et al. (2001a); tec00: Tecza et al. (2000). Col. (9), adopted morphology class, a: wide binary; b: close binary; cde: single merger (either diffuse merger, compact merger, or old merger); iso: isolated system; m: multiple mergers. Symbols: H = star-forming galaxies, L = LINERs, S2 = Seyfert 2 galaxies, S1 = Seyfert 1 galaxies, cp = starburst-AGN composite galaxies. Col. (10): $\log(L_{\text{IR}}/L_{\odot})$, data from Kewley et al. (2001a).

TABLE 4
SPECTRAL CLASSIFICATION AS A FUNCTION OF L_{IR} FOR THE 1 JY ULIRG + BGS
SAMPLES

spectral type	$\log(L_{\text{IR}}/L_{\odot})$			
	< 11	11–11.99	12–12.29	12.3–12.8
new classification, excluding double nuclei objects, 3-of-3 criterion				
Total number	22	51	69	31
starburst	8(36.4%)	12(23.5%)	3(4.3%)	1(3.2%)
starburst-AGN composite	8(36.4%)	19(37.3%)	33(47.8%)	12(38.7%)
Seyfert 2	1(4.5%)	7(13.7%)	13(18.8%)	8(25.8%)
Seyfert 1	0(0%)	1(2%)	2(2.9%)	8(25.8%)
LINER	2(9.1%)	3(5.9%)	3(4.3%)	0(0%)
Ambiguous	3(13.6%)	9(17.6%)	15(21.7%)	2(6.5%)
new classification, excluding double nuclei objects, 2-of-3 criterion				
Total number	22	51	69	31
starburst	10(45.5%)	12(23.5%)	7(10.2%)	1(3.2%)
starburst-AGN composite	8(36.3%)	19(37.3%)	33(47.8%)	12(38.7%)
Seyfert 2	2(9.1%)	16(31.3%)	24(34.8%)	10(32.3%)
Seyfert 1	0(0%)	1(2%)	2(2.9%)	8(25.8%)
LINER	2(9.1%)	3(5.9%)	3(4.3%)	0(0%)

NOTE. — Number of galaxies and their fraction (shown in brackets) in each spectral type class. Top rows are results from the 3-of-3 criterion (not including galaxies with double nuclei); bottom rows are results from the 2-of-3 criterion (not including galaxies with double nuclei).

TABLE 5
SPECTRAL CLASSIFICATION AS A FUNCTION OF L_{IR} FOR THE SW01 SAMPLE

spectral type	$\log(L_{\text{IR}}/L_{\odot})$			
	8.0–10.19	10.2–10.69	10.7–11.09	11.1–12.2
new classification, excluding double nuclei objects, 3-of-3 criterion				
Total number	37	49	49	41
starburst (HII region)	25(67.6%)	25(51.0%)	15(30.6%)	5(12.2%)
starburst-AGN composite	7(18.9%)	13(26.5%)	19(38.8%)	15(36.5%)
Seyfert 2	4(10.8%)	8(16.3%)	7(14.3%)	14(34.2%)
Seyfert 1	0(0%)	2(4.1%)	3(6.1%)	5(12.2%)
LINER	1(2.7%)	0(0%)	1(2.0%)	0(0.0%)
Ambiguous	0(0%)	1(2.1%)	4(8.2%)	2(4.9%)

NOTE. — Since the fraction of ambiguous galaxies in SW01 is small, we only list the stringent 3-of-3 criterion results here. Detail classification for a specific ambiguous galaxy can be found in Table 1.

TABLE 6
SPECTRAL TYPE AS A FUNCTION OF MORPHOLOGY FOR THE 1 JY ULIRG SAMPLE

Spectral type	Morphology Group ^a				
	Wide binary	Close binary	Diffuse merger	Compact merger	Old merger
Total number	17	29	15	30	11
starburst	2(11.8%±8.3%)	5(17.2%±7.7%)	0(0%±0%)	0(0%±0%)	0(0%±0%)
starburst-AGN composite	8(47%±16.7%)	16(55.2%±13.7%)	12(80.0%±23.1%)	11(36.6%±11.1%)	4(36.4%±18.1%)
LINER	0(0%±0%)	2(6.9%±4.9%)	1(6.7%±6.7%)	0(0%±0%)	0(0%±0%)
Seyfert 2	7(41.2%±15.6%)	6(20.7%±8.4%)	2(13.3%±9.4%)	11(36.7%±11.1%)	5(45.4%±20.3%)
Seyfert 1	0(0%±0%)	0(0%±0%)	0(0%±0%)	8(26.7%±9.4%)	2(18.2%±12.9%)

^a Notes: The 1 isolated object and 5 possible triple-system objects are not included here. The mean and standard error of the fractions are shown in the brackets.

TABLE 7
SPECTRAL TYPE AS A FUNCTION OF MORPHOLOGY FOR THE LIRGS IN THE BGS SAMPLE

Spectral type	Morphology Group ^a			
	Wide binary	Close binary	Single merger	Isolated
Total number	20	13	9	35
starburst	8(40.0%)	6(46.1%)	4(44.5%)	12(34.3%)
starburst-AGN composite	9(45.0%)	5(38.5%)	3(33.3%)	15(42.9%)
LINER	0(0%)	1(7.7%)	1(11.1%)	3(8.6%)
Seyfert 2	2(10.0%)	1(7.7%)	1(11.1%)	5(14.2%)
Seyfert 1	1(5.0%)	0(0%)	0(0%)	0(0%)

NOTE. — Only 77 objects with both available spectral type and morphology classification are included.

^a Notes: wide binary ($n_s > 10$ kpc); close binary ($n_s < 10$ kpc); single merger: merger in the final merging stage where the two nuclei have merged into a single one; isolated non-merging systems.

TABLE 8
SPECTRAL TYPE AS A FUNCTION OF MORPHOLOGY FOR THE SW01 SAMPLE

Spectral type	Morphology Group ^a			
	Wide binary	Close binary	Single merger	Isolated
Total number	41	24	18	124
starburst (HII region)	15(36.6%)	14(58.4%)	5(33.3%)	55(46.2%)
starburst-AGN composite	14(34.2%)	5(20.8%)	5(33.3%)	37(31.1%)
LINER	0(0%)	2(8.3%)	0(0%)	1(0.8%)
Seyfert 2	9(21.9%)	2(8.3%)	5(33.3%)	22(18.5%)
Seyfert 1	3(7.3%)	1(4.2%)	0(0%)	4(3.4%)

NOTE. — Only 207 objects with both available spectral type and morphology classification are included.

^a wide binary ($n_s > 10$ kpc); close binary ($n_s < 10$ kpc); single merger: merger in the final merging stage where the two nuclei have merged into a single one; isolated non-merging systems.

TABLE 9
PROPERTIES OF LINERS IN THE 3 SAMPLES

Name	$d_{[\text{OI}]}$ ^a (dex)	$d_{[\text{SII}]}$ (dex)	$\log(L_{\text{IR}}/L_{\odot})$	morphology
1 Jy ULIRGs				
IRAS14504-1958	0.05	0.02	12.12	...
IRAS04074-2801	0.15	0.18	12.14	diffuse merger
IRAS15327+2340(Arp220)	0.31	0.34	12.17	close binary, $n_s = 0$. kpc
SW01				
IRAS05497-0728(NGC2110)	0.07	0.08	10.08	...
IRAS16504+0228(NGC6240)	0.4	0.28	10.86	close binary, $n_s = 0.74$ kpc
IRAS16399-0937,object2	0.05	0.08	11.07	...
BGS				
IRAS05187-1017	0.17	0.12	11.23	isolated?
IRAS01364-1042	0.35	0.05	11.76	...
IRAS03134-0236(NGC1266)	0.13	0.44	10.34	isolated?
IRAS22359-2606(ESO534-G009)	0.54	0.32	10.61	isolated?

NOTE. — General properties of the 9 LINERs classified by the new scheme in the three samples.

^a index distance from the Seyfert-LINER classification line in the BPT [O I]diagram. Available morphology information comes from images in NED.

TABLE 10
SPECTRAL TYPE AND D_{AGN}

Spectral type	D_{AGN}	
	Mean	Median
starburst (HII region)	0.2(0.2)	0(0.2)
starburst-AGN composite	0.4(0.4)	0.3(0.4)
LINER	0.8(0.8)	0.9(0.9)
Seyfert 2	0.8(0.7)	0.8(0.7)

NOTE. — Col. (1) Spectral Types defined using the Ke06 semi-empirical scheme; Col. (2) D_{AGN} median value; Col. (3) D_{AGN} mean value. Based on 420 galaxies from the 1 Jy ULIRG, BGS and SW01 samples. Seyfert 1 objects are set to have $D_{\text{AGN}} \equiv 1$.